Structure of the II2-III$_2$-IV2 mitochondrial supercomplex from the parasite *Perkinsus marinus*

Fēi Wú[1], Alexander Mühleip[2], Thomas Gruhl[3,6], Lilach Sheiner[4,*], Amandine Maréchal[3,5,*], Alexey Amunts*

[1] Science for Life Laboratory, Department of Biochemistry and Biophysics, Stockholm University, 17165 Solna, Sweden.

[2] Institute of Biotechnology, Helsinki Institute of Life Science, University of Helsinki, Finland

[3] Institute of Structural and Molecular Biology, Birkbeck College, London, UK.

[4] Wellcome Centre for Integrative Parasitology, University of Glasgow, UK.

[5] Institute of Structural and Molecular Biology, University College London, London, UK.

[6] current address: PCR Biosystems, London, UK.

* correspondence: Lilach.Sheiner@glasgow.ac.uk, a.marechal@ucl.ac.uk, alexey.amunts@gmail.com

Respiratory complexes have co-evolved into supercomplexes in different clades to sustain energy production at the basis of eukaryotic life. In this study, using cryogenic electron microscopy, we determined the 2.1 Å resolution structure of a 104-subunit II2-III2-IV2 supercomplex from the parasite Perkinsus marinus, related to Apicomplexa, capable of complete electron transport from succinate to molecular oxygen. A feature of the parasite is the association of two copies of complex II via the apicomplexan subunit SDHG that interacts with both complexes III and IV and bridge the supercomplex. In the c_1 state, we identified two protein factors, ISPR1 and ISPR2 bound on the surface of complex III, where Cytochrome *c* docks, acting as negative regulators. The acquisition of 15 specific subunits to complex IV results in its lateral offset, increasing the distance between the Cytochrome *c* electron donor and acceptor sites. The domain homologous to canonical mitochondria-encoded transmembrane subunit COX2 is made of three separate polypeptides encoded in the nucleus, and their correct assembly is a prerequisite for electron transport in the supercomplex. Subunits Cytochrome *b* and COX1 comprise a +2 frameshift introduced during protein synthesis by the mitoribosome. Among 114 modelled endogenous lipids, we detect a direct contribution to the formation of the divergent supercomplex and its functional sites, including assembly of CII and ubiquinone binding. Together, our findings expose the uniqueness of the principal components of bioenergetics in the mitochondria of parasites.

Eukaryotes rely on oxidative phosphorylation and the crucial energy conversion provided by encapsulated mitochondria for their aerobic metabolism. This occurs through respiratory chains and the coupled transport of electrons and protons across multi-protein complexes embedded in the inner mitochondrial membrane (IMM), ultimately leading to adenosine triphosphate (ATP) synthesis. While these respiratory complexes were initially characterised individually, it is now evident that many of them can assemble into higher organisational order assemblies termed supercomplexes (SCs). Functionally, SCs can facilitate complete electron transport from nicotinamide adenine dinucleotide (NADH) to molecular oxygen. At least four different stoichiometries and composition types of SCs have been reported *in situ* across various regions of the mammalian mitochondrial membrane [1], containing complex I (CI, NADH:ubiquinone oxidoreductase), III_2 (CIII, ubiquinol:cytochrome *c* oxidoreductase or cytochrome bc_1) and IV (CIV, cytochrome *c* oxidase). To date, no mammalian SC has been identified to contain complex II (CII, succinate:UQ oxidoreductase). In humans, different stoichiometries of SCs have been associated with metabolic state changes [2,3] and diseases [4,5]. In other organisms, SCs can reach a molecular weight of 10 MDa, and recent studies have highlighted their central role in mitochondrial ultrastructure and function [6–9].

The respiratory chains of parasites likely exhibit noticeable functional and compositional distinctions, which have not been fully investigated and may be linked to disease. In addition, parasitic microorganisms possess some of the most reduced and divergent mitochondrial DNA [10,11], making them intriguing for insights into less conventional modes of life. Particularly, the mitochondria of the infectious Apicomplexa parasites display unique cristae morphology shaped by the ATP synthase cyclic hexamers localised to curved apical membrane regions [12]. Although these parasites lack CI, proteomic analysis of their CII, CIII and CIV has revealed significant compositional differences, with many detected subunits being previously unknown, suggesting a potentially unique protein organisation [13,14]. Understanding the principles of electron transport in these complexes is crucial for parasite physiology and potential therapeutic interventions targeting energy production. However, fundamental mechanistic aspects in parasites have remained elusive due to a lack of corresponding structural information, including respiratory complexes organisation. We thus set to determine the atomic structures of noncanonical SCs and identify specific factors underlying their unique characteristics.

Here, we report 2.1-2.4 Å resolution structures of the mitochondrial II2-III_2-IV2 SC from the parasite *Perkinsus marinus* that infects molluscs and is related to Apicomplexa, using cryogenic-electron microscopy (cryo-EM). We show that, in addition to CIII and CIV, two monomers of functional CII are associated with the SC, resulting in a stoichiometric II2-III_2-IV2 that has not been observed in any other organism. This SC is capable of electron transport from succinate to oxygen, and represents a new type of functional respirasome. The data enabled visualization of native lipids with key roles in SC formation and activity. Finally, we identified an associated heterodimer factor as a potential regulator of CIII locking the Rieske iron-sulfur protein (RIP1) head in the c_1-state, which we named Iron-Sulfur Protein Related (ISPR1,2).

Results

The parasite SC is a new type of stoichiometric respirasome

To study mitochondrial SCs in parasite mitochondria, we used an intracellular pathogen model *P. marinus* from the Phylum Perkinsozoa representing an early branch of the myzozoan lineage and related to Apicomplexa, sharing morphological characteristics [15]. To keep the complexes in a close-to-native environment and elucidate any intact SC assembly, we minimised the purification procedure. Upon mitochondria solubilisation with the mild detergent digitonin, we employed a single step of sucrose density cushion to separate the heavy components of the solubilized mitochondrial membranes. This material was subjected to native polyacrylamide gel electrophoresis (PAGE) which revealed several bands at apparent molecular weights above 720 kDa. In-gel activity assay for CIV highlighted the presence of respiratory CIV in only one assembly, the one of highest molecular weight (migrating close to 1 MDa) (Fig. S1a). The redox absorption spectrum of this sample recorded in the visible range showed presence of A-, B- and C-type hemes, characteristic of presence of respiratory complexes III and IV (Fig. S1b). The functional integrity of the CIV-containing SC was assessed polarographically using an oxygen electrode (Fig. 1a). The SC sample is active and reduces molecular oxygen at a rate of 22 ± 3 $e.s^{-1}$ using succinate as a substrate (Fig. S1c). Addition of exogenous cytochrome *c* (Cyt *c*), but not ubiquinone, was required for activity which supports co-purification of the latter, but not of the former (Fig. 1a). The addition of the CII inhibitor malonate stops oxygen reduction and the reaction can be resumed by addition of reduced quinone to feed electrons directly to CIII (Fig. 1a). The initial III-IV rate (42 ± 13 $e.s^{-1}$) is faster than the II-IV rate and is inhibited by the CIII inhibitor antimycin A. Subsequent addition of ascorbate and TMPD allowed recording of the CIV rate at 81 ± 31 $e.s^{-1}$, which is sensible to potassium cyanide (KCN) (Fig. 1a, Fig. S1c). Thus, in the parasite SC electrons are transferred from CII to CIII to CIV.

Since this preparation contained a mixture of high molecular weight assemblies, for structural studies, we separated them on a gel filtration column (Fig. S2a). This allowed us to reconstruct the distinctive ATP synthase hexamers (Fig. S2b) and confirm this fundamental feature of apicomplexan parasites [12]. We then focused on the SC particles, which led to the reconstruction of the II2-III_2-IV2 SC at an overall resolution of 2.1 Å, and the local resolution was further improved by performing masked refinements around CII2$CIII_2$, CIV, and CII (Fig. S2c,d; Fig. S3; Tables S1, S3). The resulting model for the entire SC consists of 104 protein subunits, 114 lipids, and 42 co-factors for a total mass of 1.8 MDa (Fig. 1b,c; Fig. S4; Video S1, Table S3).

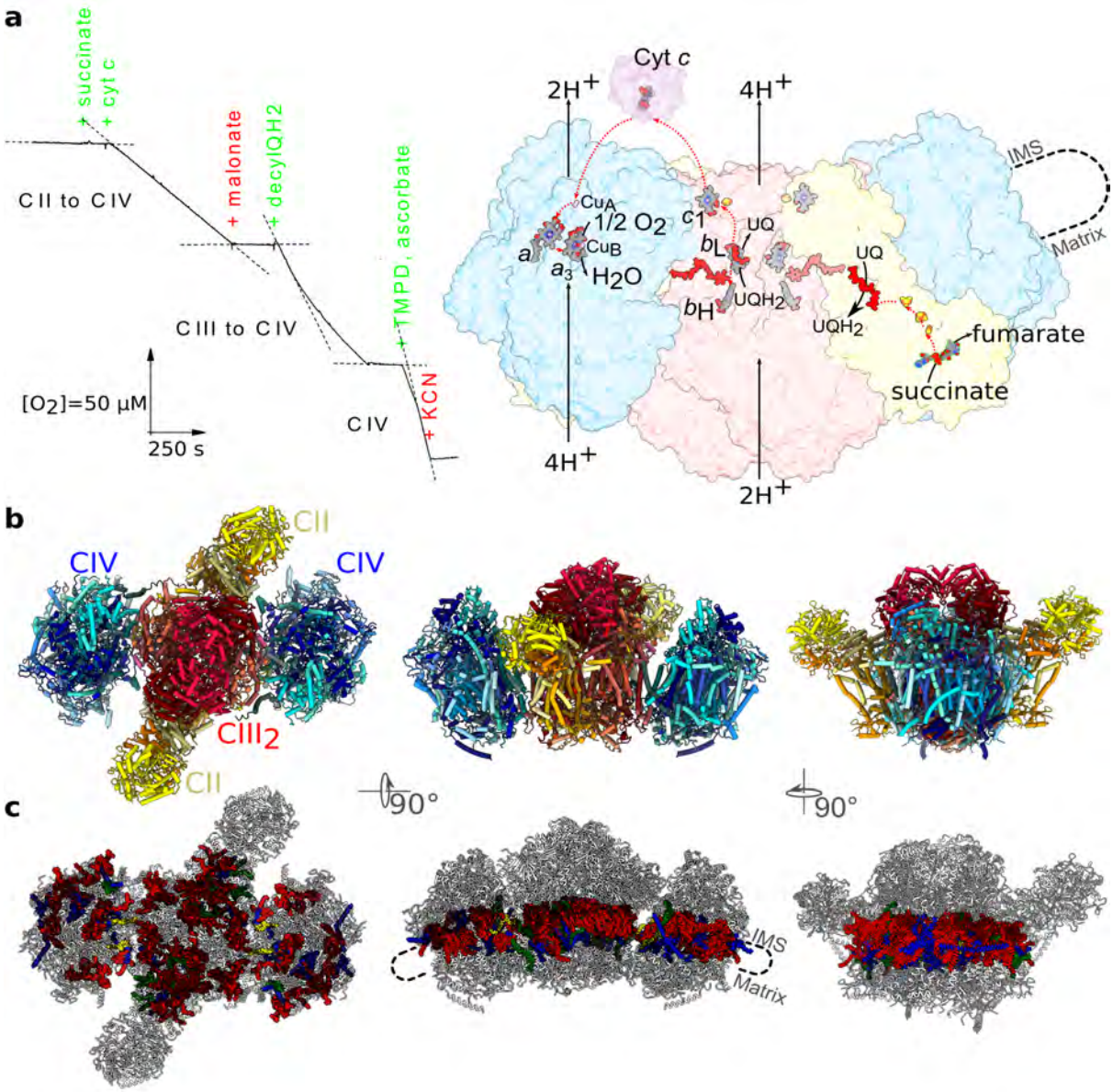

Fig. 1 Structure of the II2-III$_2$-IV2 supercomplex. a, Left, oxygen-consumption assay showing electron transport from succinate (via CII) and decylquinol (via CIII) to molecular oxygen (CIV). Substrates and inhibitors for the reactions are displayed in green and red, respectively. Right, Redox cofactors and electron transfer routes (red lines) underpinning the SC activity. **b,** Matrix (left) and membrane (middle and right) views of the SC model showing how CII, CIII$_2$ and CIV are arranged with respect to each other. **c,** Overview of the 114 lipids modelled within the SC membrane domain, including 60 cardiolipins (red); 4 phosphatidic acids (yellow); 32 phosphoethanolamines (blue) and 18 phosphatidylcholines (green).

CII consisting of 4 conserved and 7 specific subunits (Fig. S5) is found in two copies stably bound in the SC. The presence of a single copy of CII was previously reported in ciliates [8], but the current arrangement in the structure of the parasite is markedly different (see below). The CIII homodimer is the most canonical of all the complexes consisting of 10 conserved and 2 specific subunits for each monomer (Fig. S6). During catalysis, the head domain of

130 RIP1 adopts conformational changes to allow electron transfer to and from the iron-sulfur
131 (FeS) cluster [16]. We detected three distinct states for RIP1 in the SC and refined them to the
132 resolution of 2.2 Å (state *b*), 2.5 Å (state c_1) and 2.4 Å (intermediate) (Fig. S2d; Fig. S3b; Ta-
133 bles S1,S2). In the c_1-state, the electron acceptor, Cyt *c*, docking site is occupied by a protein
134 heterodimer that has not been previously reported and assigned directly from our cryo-EM
135 density map to ISPR1 and ISPR2 (Fig S7). Two copies of CIV, each consisting of 12 con-
136 served and 15 specific subunits (Fig. S8), flank the SC and appear to be more flexible. We
137 masked and refined CIV to the local resolution of 2.2 Å (Fig. S2a, Table S1). Finally, we fur-
138 ther studied potential conformational changes by applying a multi-body refinement analysis,
139 which indicated continuous motion in the two eigenvectors defined by combinations of CIV
140 rotation with respect to CIII (Fig. S9).
141

142 **Structural characterisation of the II2-III$_2$-IV2 mitochondrial supercomplex**

143 Our structure reveals an architecture of the III:IV interface that is mediated by parasite-spe-
144 cific subunits and influenced by the presence of CII. CIV is oriented almost perpendicular to
145 the CIII dimer axis (Fig. 1b). Examination of the III:IV interface (Fig. 2a) shows that it is
146 formed by six apicomplexan subunits of CIV, COX31, 33, 34, 36, 39 and COX40, and two
147 canonical subunits, COX2B and COX6B, making the interface substantially larger than in
148 previously reported III-IV SC structures [17–21]. Most of the interactions formed by the apicom-
149 plexan subunits are in the intermembrane space (IMS) between a single CIV copy and one
150 CIII monomer (Fig. 2a,b), resulting in a V-shape arrangement of the complexes that contrib-
151 utes to the local curvature of the membrane (Fig. S10a). Within the IMM, two single-trans-
152 membrane apicomplexan subunits, COX39 and COX40, form a helical bundle with QCR8
153 which is further supported by protein-lipid-protein interactions (Fig. S10b). A striking feature
154 is that in the matrix, COX36 extends to the second CIII monomer via its subunit QCR7 (Fig.
155 2a). COX36 is a peripheral protein consisting of three domains: a C-terminal tail (residues
156 36-93) that anchors it to the CIV core in the IMS, a transmembrane α-helix (residues 10-35)
157 that is tilted by 13° towards the second CIII monomer, and the N-terminus that forms five in-
158 ter-complex interactions with QCR7 (Fig. 2d). This highlights a key role of the Apicomplexa
159 specific COX36 subunits in tying the SC at the altered interacting surface (Fig. S11). Conse-
160 quently, the overall III:IV interface includes both CIII monomers facing CIV, and a different
161 type of SC is formed via intricate interactions of parasite-specific subunits. This is illustrated
162 by the laterally offset CIV compared to known fungi [17,18], plant [19] and mammalian [22,23] SCs
163 (Fig. S12).

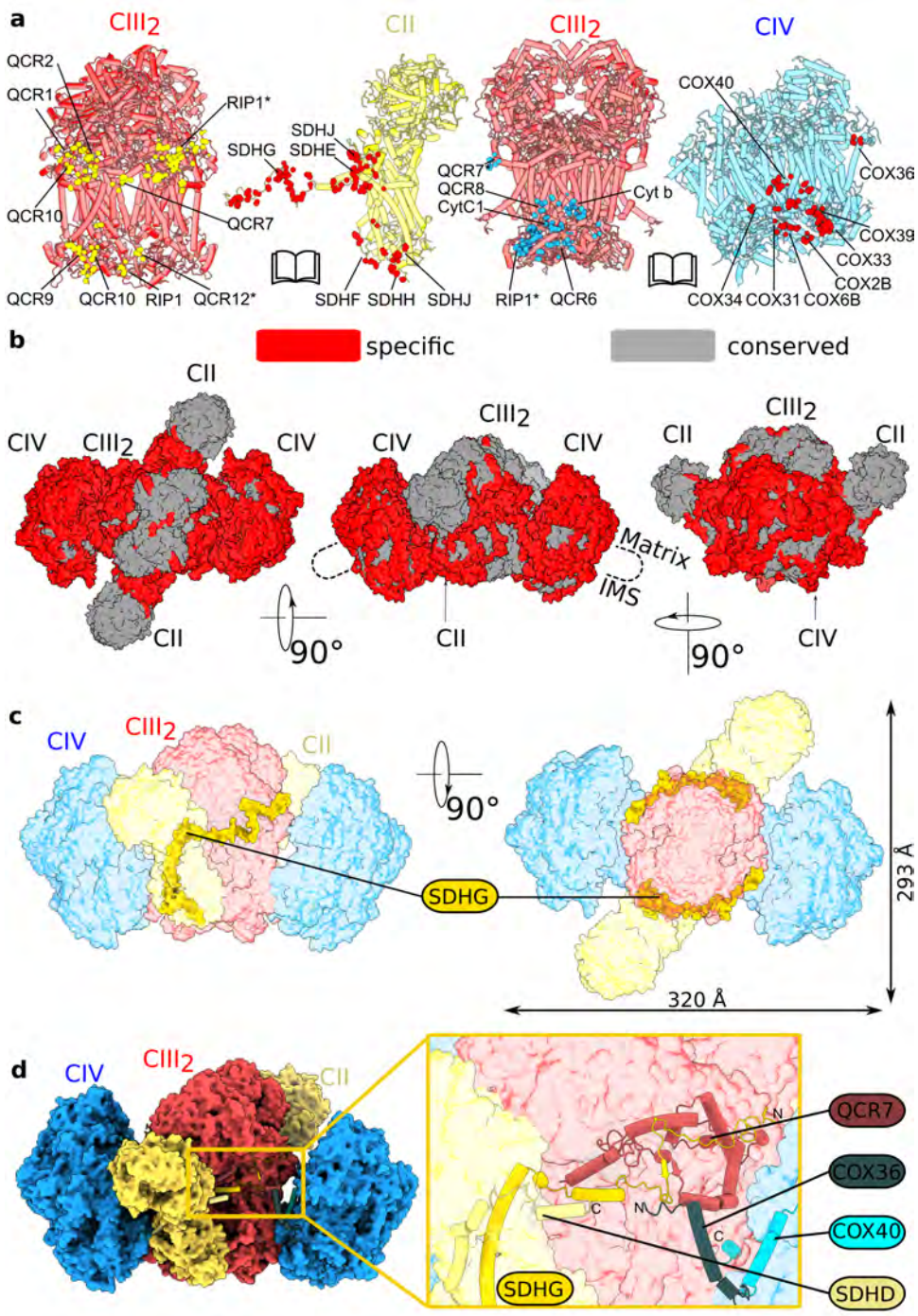

Fig. 2 The association of CII with CIII and CIV. a, Open book views highlighting the contact sites of $CIII_2$ with CII (left), and $CIII_2$ with CIV (right). Interactions are shown as spheres (CII in yellow, $CIII_2$ in red, CIV in blue). CII interacts with one CIII monomer, whereas each CIV copy interacts with both CIII monomers. **b,** The specific and conserved subunits are shown in red and grey, respectively, illustrating that the extensive contacts between complexes occur through their specific subunits, providing large interfaces in the SC. **c**, Membrane and matrix views highlighting how the N-termini of CII subunit SDHG (dark yellow) wrap around $CIII_2$. **d,** SDHD and SDHG (light and dark yellow cartoon) helix bundle docks CII to CIII and CIV. Close-up view illustrating protein subunits and contact sites between the three complexes, where SDHG forms a parallel beta-sheet with QCR7 from CIII and interacts with COX36 from CIV.

175 The association of CII in the SC represents another feature of the structure. *P. marinus* CII
176 has ten subunits, four conserved and six apicomplexan (Fig. S6). On the matrix side of the li-
177 pid bilayer, CII contains an amphipathic arm that protrudes towards CIII (Fig. 2c,d). The arm
178 consists of a 13-amino acid-long helix of the apicomplexan SDHG (residues 68-80) that
179 forms a bundle with the N-terminal extension of QCR7 (residues 4-17). Both interact with
180 cardiolipin CDL26, highlighting the importance of co-purification of native lipids (Fig. S13).
181 On the opposite side, it is stabilized by the C-terminal helix of SDHD, another parasite spe-
182 cific extension, via cardiolipin CDL19 (Fig. S13). Together, this arrangement stabilises the
183 N-terminal region of SDHG that further wraps around CIII, engaging with RIP1 N-terminal
184 extension over the distance of ~45 Å (Fig. 2c). Here, SDHG (residues 49-51) also forms a
185 parallel beta sheet with CIII subunit QCR7 (residues 28-30) and interacts with CIV subunit
186 COX36 (N-terminal residues 1-9) (Fig. 2d, Fig. S11). Thus, all three complexes are bridged
187 in this region of the SC.

188 Our structure additionally reveals that the membrane domain of *P. marinus* CII is does not
189 hold a coordination site for a heme group as seen in other mitochondrial forms of the enzyme,
190 including in mammals, where axial ligands are provided by the canonical subunits SDHC-
191 SDHD. SDHC-SDHD were not previously identified in Apicomplexa due to their divergent
192 and truncated sequences. Subunit SDHC (5.5 kDa) is shortened in our structure, representing
193 the only protein that is found in a reduced form in the entire SC (Fig. S14a). Subunit SDHD
194 (8.0 kDa) could only be assigned by locating topologically conserved transmembrane helices
195 in the map. Consequently, the canonical heme-binding module adopts a different confor-
196 mation, and no density for the prosthetic group could be found in our structure (Fig. S14a).

197

198 **Conformational dynamics of CIII and CIV in the supercomplex**

199 To explore potential conformational changes relating to function, we applied multi-body re-
200 finement analysis using CIII and CIV as individual bodies (Fig. S9). The analysis revealed
201 continuous motions describing a movement of CIV in relation to CIII (Fig. S9b). The intrin-
202 sic flexibility is defined by combinations of all rotations of CIV up to 11° (Fig. S9c). The ro-
203 tations affect the distance between the electron donor and acceptor sites on CIII and CIV, re-
204 spectively, where the electron carrier Cyt *c* docks. In the consensus model, the distance be-
205 tween the Cyt *c* docking sites on CIII and CIV is ~79 Å (Fig. S15a). The maximum distance
206 in the extreme states of component 1 in multi-body analysis is 84 Å and is shortened to 77 Å
207 when maximal rotation around the pivot points is achieved (Fig. S9c). This is longer than the
208 60 Å measured in the yeast III-IV SC [17,18]. Moreover, unlike in yeast, no strongly negatively
209 charged path is observed at the surface of our SC structure that would facilitate the 2D diffu-
210 sion of Cyt *c* between CIII and CIV [24] (Fig. S15b). Finally, in addition to the increased dis-
211 tance and altered surface charge, Apicomplexan subunits also form a physical obstacle for 2D
212 diffusion (Fig. S15b). The conformational dynamics seen are primarily realised in our struc-
213 ture due to the COX39-COX40-QCR8 bundle at the interface, where cardiolipin CDL31 and
214 lipid phosphate phosphatase LPP504 are resolved (Fig. S10b). The COX40 transmembrane
215 helix assists the two complexes in maintaining the flexible membrane contacts when in the
216 extreme conformation that reduces the distance between the donor and acceptor sites for Cyt

217 *c* given the structural constraints. Peripheral interactions of both CIII monomers with each
218 CIV copy further help stabilising the overall structure (Fig. 2b, Fig. S11).
219

220 **Identification of ISPR1 and ISPR2 on $CIII_2$ in the *c1*-state**

221 On quinol oxidation, electron transfer within CIII is bifurcated, and it is the c_1 branch that
222 leads to reduction of Cyt *c*. This occurs through conformational changes of the RIP1 protein
223 head in the IMS. RIP1 is a transmembrane protein incorporated into $CIII_2$ as the last matura-
224 tion step to provide catalytic activity to the enzyme [25]. In mammals, RIP1 forms a complex in
225 the matrix with a protein derived from its own mitochondrial precursor [26]. In our structure,
226 the mammalian mitochondrial precursor is absent, and Apicomplexa specific protein QCR11
227 occupies its position, interacting with RIP1 in the matrix (Fig. S16).

228 To elucidate the conformational changes of the RIP1 head domain, we employed masks and
229 classified reconstructions (Fig. S2d, S3b). This revealed three conformations of RIP1 with re-
230 spect to CIII with distances between the FeS cluster and heme c_1 measured as 7.4 Å (c_1-state),
231 9.6 Å (intermediate), and 23.8 Å (*b*-state), while the corresponding distances between the UQ
232 bound at the Qo site and the FeS cluster were 23.2 Å, 24.2 Å, and 8.1 Å. In the c_1-state, com-
233 prising 38% of particles, we locally refined the rotated head area to 2.9 Å resolution, reveal-
234 ing additional protein density on each CIII monomers surrounding the RIP1 head domain in
235 the IMS (Fig. S3b).

236 We initially constructed a polyamine backbone model into this density and estimated proba-
237 ble residue identities based on the map using *Coot* v0.9 [27,28]. Predicted sequences were then
238 queried against mass spectrometry data (Supplementary Data file), with the highest-weighted
239 spectra displaying a sequence represented by only three unique peptides covering 25% of
240 amino acids. We surmised that the protein database might be poorly annotated, prompting us
241 to query the predicted sequences directly against open reading frames using BLASTP [29]. This
242 approach identified the shotgun sequences scf_1104296932410 1 749426 1 (https://pro-
243 tists.ensembl.org/Perkinsus_marinus_atcc_50983_gca_000006405/Loca-
244 tion/View?db=;r=scf_1104296932410:1-749426) and scf_1104296971434 1 346455 1
245 (https://protists.ensembl.org/Perkinsus_marinus_atcc_50983_gca_000006405/Loca-
246 tion/View?db=;r=scf_1104296971434:1-346455), which we named ISPR1 and ISPR2 due to
247 their association with the iron-sulfur protein. The major difference between ISPR1 and ISPR2
248 is in their termini. ISPR1 has an extra density corresponding to 27 residues at the C-terminus,
249 and ISPR2 has an extra density corresponding to 42 residues at the N-terminus (Fig. S7).
250 Thus, they are present as a heterodimer of a long isoform 1 (179 amino acids) and a short iso-
251 form 2 (153 residues). The sequence of *P. marinus* (ATCC 50983) contains entries
252 Pmar_PMAR022267 and Pmar_PMAR010955 covering 58% and 41% of the ISPR1 and
253 ISPR2 modelled sequences with >90% identity. In addition, *Perkinsus Olseni* (ATCC PRA-
254 207) contains entries FOZ63_010970 and FOZ60_003022 covering 100% and 99% of the
255 ISPR1 and ISPR2 modelled sequences with 65% and 80% identity. Both data have been used
256 as reference for model building. We also found homologs for ISPR1 and ISPR2 in *Symbio-*
257 *dinium*, *Cyclospora*, *Toxoplasma* and *Neospora* species (Fig. S17a). TGME49_224932 from
258 *Toxoplasma browser* has three homologous regions to ISPR, as well as an extended C-

terminus (Fig. S17b). It is noteworthy that homolog search is challenging in Apicomplexa due to diverged sequences and a poorly annotated database [30].

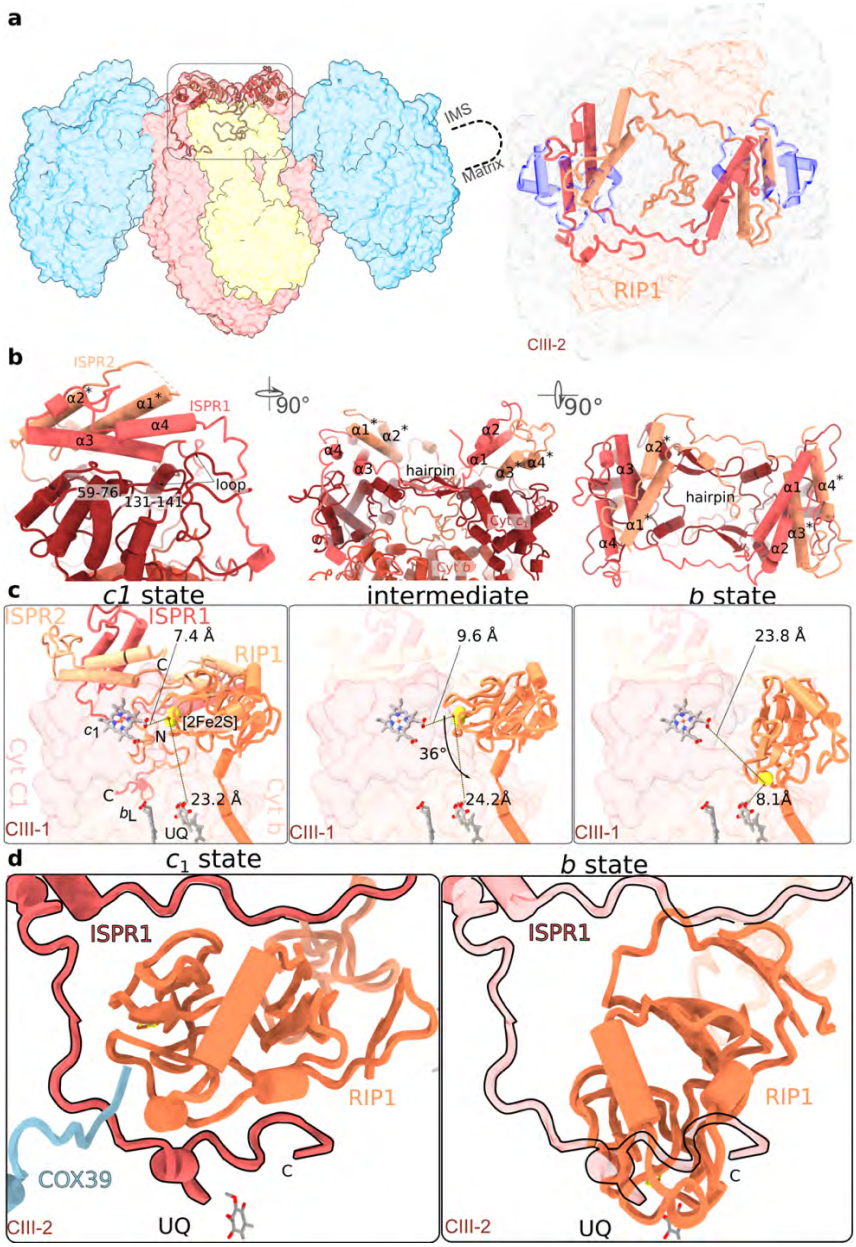

Fig. 3 Heterodimer ISPR1, ISPR2 occupies the Cyt *c* binding site on CIII and locks it in c_1 state. a, ISPR1 (light red) and ISPR2 (orange) in the Cyt *c* binding site. ISPR2 N-terminus fills the cavity in the IMS between the monomers of CIII, whereas ISPR1 C-terminus contacts RIP1. Superposition of the Cyt *c* (transparent purple) from the $CIII_2$-bound structure (PDB ID: 1KYO) shows that the ISPR dimer compete for the same site. **b,** ISPR1 and ISPR2 contact sites on Cyt c_1 (brown) and Cyt *b* (tomato). **c,** Three distinct conformations (c_1 state, intermediate and *b* state) are identified by classifying the head domain of RIP1. The distances between redox centers c_1, FeS, and UQ are shown. The ISPR dimer is present in the c_1 state only, and its position is indicated with transparent cartoon in the intermediate and *b* state. **d,** In c_1-state, ISPR1 C-terminus locks RIP head by hampering its rotation, effectively preventing electron transfer from UQ to FeS. In *b*-state, the position of ISPR1 C-terminus indicated with transparent cartoon would clash with RIP1 head domain.

ISPR heterodimer occupies the docking site of the electron carrier Cyt *c* and locks $CIII_2$ in the c_1-state

Endogenous ISPR1 and ISPR2, co-purified in our structure, comprise two pairs of associated helices (α1-α2, α3-α4) separated from each other by ~35 Å (Fig. 3a). Together, they forms two pseudo symmetrical four-helix bundles, where α1-α2 of one monomer is associated with α3-α4 of the other monomer (Fig. 3b). The *AlphaFold2* [31] prediction of the heterodimer using protein sequences based on the density map generates a similar secondary structure model of helical bundles, however, due to the presence of loop linkers between the helices, the ternary prediction differs slightly from our experimental model.

ISPR1,2 binds to $CIII_2$ through the solvent-exposed side of the conserved transmembrane subunits Cyt c_1 and Cyt *b*. Cyt c_1 provides a surface area of 1150 $Å^2$ for a tight association with ISPR-α1 and α2 via four contacts (Fig. 3b): 1) loops regions 180-182 and 196-203 positioned between α1 and α2; 2) helix formed by residues 59-76 approaching the middle of α2 from the membrane plane; 3) short helix (residues 134-141) associated perpendicularly with α2 at its bending point (100°), and thus incompassed by the latter; 4) β-hairpin 105-120 that extends ~20 Å in parallel to the α2-α3 loop (Fig. 3b). This loop leads to α3 and α4 on the opposite side that are associated on top of α1 and α2 of the other monomer, together forming the heterodimer (Fig. 3b).

In addition, ISPR1 interacts with the RIP1 head domain via residues 67-75 and the C-terminal extension (residues 138-160) running for 25 Å in the cleft between RIP1 head and Cyt *b* (Fig. 3b,c). In proximity to the ISPR1 C-terminal extension, COX39 (CIV) C-terminus engages with the head domain of RIP1. Thereby, RIP1 is locked in the c_1 state (Fig. 3b,c; Video S1). ISPR2 interacts with RIP1 from the other monomer mainly via residues 105-122 and weakly via the C-terminal region, due to its shorter length compared to ISPR1. From the other side, ISPR2 N-terminus (residues 2-46) inserts into the dimer axis of Cyt *b* close to the membrane surface, aligning with the C2 symmetry of the entire SC (Fig. 3a). The N-terminal segment of ISPR2 can be further divided into two regions: the flexible linker region (residues 17-46), which traverses the central cavity of $CIII_2$, and the stable axis region (residue 2-16), positioned along the C2 axis of the dimer (Fig. 3a). Thus, the ISPR1 C-terminus stabilises RIP1 head in the c_1 state, and ISPR2 N-terminus further associates the heterodimer in the Cyt *c* binding site. All those interactions involve regions that are generally conserved in CIII (Fig. S6).

During the transition from state c_1 to state *b*, RIP1 rotates 36°, so that the surface area for contact with ISPR1 moves towards UQ at the Qo site (Fig. 3c). The superposition of the two states shows that in state *b* RIP1 is positioned with its iron-sulfur head domain where ISPR1 C-terminus resides in the c_1-state. Thus, the two entities would clash, and the presence of ISPR is not compatible with RIP1 in state *b*, effectively blocking the Q-cycle and preventing ubiquinol oxidation altogether. The binding of ISPR1,2 involves relatively weak electrostatic interactions compared to Cyt *c* (Fig. S15c), suggesting that the electron carrier can outcompete them for the site. The antagonistic relationship of ISPR1,2 with Cyt *c* might further reflect on regulation of electron transport, which led us to reconstitute the SC-Cyt *c* for structural characterisation, however the ISPR has not been replaced, or displaced by Cyt *c* in the study. Thus, the ISPR heterodimer is stably bound to the SC in the c_1-state.

317 **Lipids in the supercomplex**

318 Lipids modulate functions of membrane proteins and specifically regulate assembly and
319 maintenance of mitochondrial SCs [32]. Moreover, cardiolipin is involved in affecting catalytic
320 activities of electron transfer that ultimately lead to apoptosis [33]. A striking feature of our
321 cryo-EM map is resolvable density for 114 lipids, and the high resolution of the reconstruc-
322 tion allowed identification of 60 cardiolipins, 4 phosphatidic acids, 18 phosphatidylcholines,
323 and 32 phosphoethanolamines (Fig. 1d, Fig. 4a-c, Video S1). Overall, the lipids surrounding
324 the II2III$_2$IV2 supercomplex show curvature toward the IMS (Fig. 1d). The identification of
325 lipids is mechanistically important because lipid molecules were shown to mediate interac-
326 tions between adjacent complexes [34,35] and thus contribute to stabilizing the SC. Particularly,
327 at the interaction interface of CII and CIII, in addition to previously mentioned CDL19 and
328 CDL26, at least four other lipids are associated with subunit SDHG, mediating intercomplex
329 interactions (Fig. 4a). In addition, at the III-IV interface, the critical interactions of QCR8
330 with COX39/COX40 are largely mediated by lipids (Fig. 4d). This likely provides overall
331 flexibility to this region and explains the relative motion of CIV in our multi-body analysis
332 (Fig. S9).

333 Lipids in our structure also refine the Q-binding pockets in CIII. Structural lipids form an ar-
334 chitecture that facilitates Q-shuttling within CIII by two means. First, at the Q_i site of CIII, an
335 elongated density is found that is not compatible with ubiquinone, suggesting that the binding
336 pocket and the channel are preoccupied in the absence of electron carrier (Fig. 4e). Therefore,
337 the structure suggests that the lipid would bind and unbind in coordination with the electron
338 carrier. Further, we observed the lipid tail of CDL15 that extends to the channel of the Qi site.
339 This provides a hydrophobic environment for ubiquinone shuttling (Fig. 4e). In addition, in
340 CIV, we observed interactions between the farnesyl tail of heme *a* and the tail of CDL 32,
341 supporting that the long hydrocarbon chain of heme *a* helps anchoring heme *a* into the hydro-
342 phobic environment (Fig. S18).

343 Finally, we show the importance of lipids in supporting the SC architecture by using *Al-*
344 *phaFold2* [31] to predict the structure of transmembrane subunits SDHG, SDHF, SDHD,
345 SDHH, SDHE, SDHJ, SDHC, and SDHI of CII and superimposing the predicted model with
346 our experimental structure that includes native lipids (Fig. S19). While the overall topology is
347 generally consistent between the prediction and the experimental model, and the soluble do-
348 mains fit reasonably well, most of the structural elements in the transmembrane region are
349 shifted or rotated (Fig. S19). The differences in the local geometry are attributed to the pres-
350 ence of native lipids that are specifically bound and woven in between the transmembrane
351 helices of CII (Fig. 4a). This underlies the importance of preserving the native membrane en-
352 vironment in structural analysis.

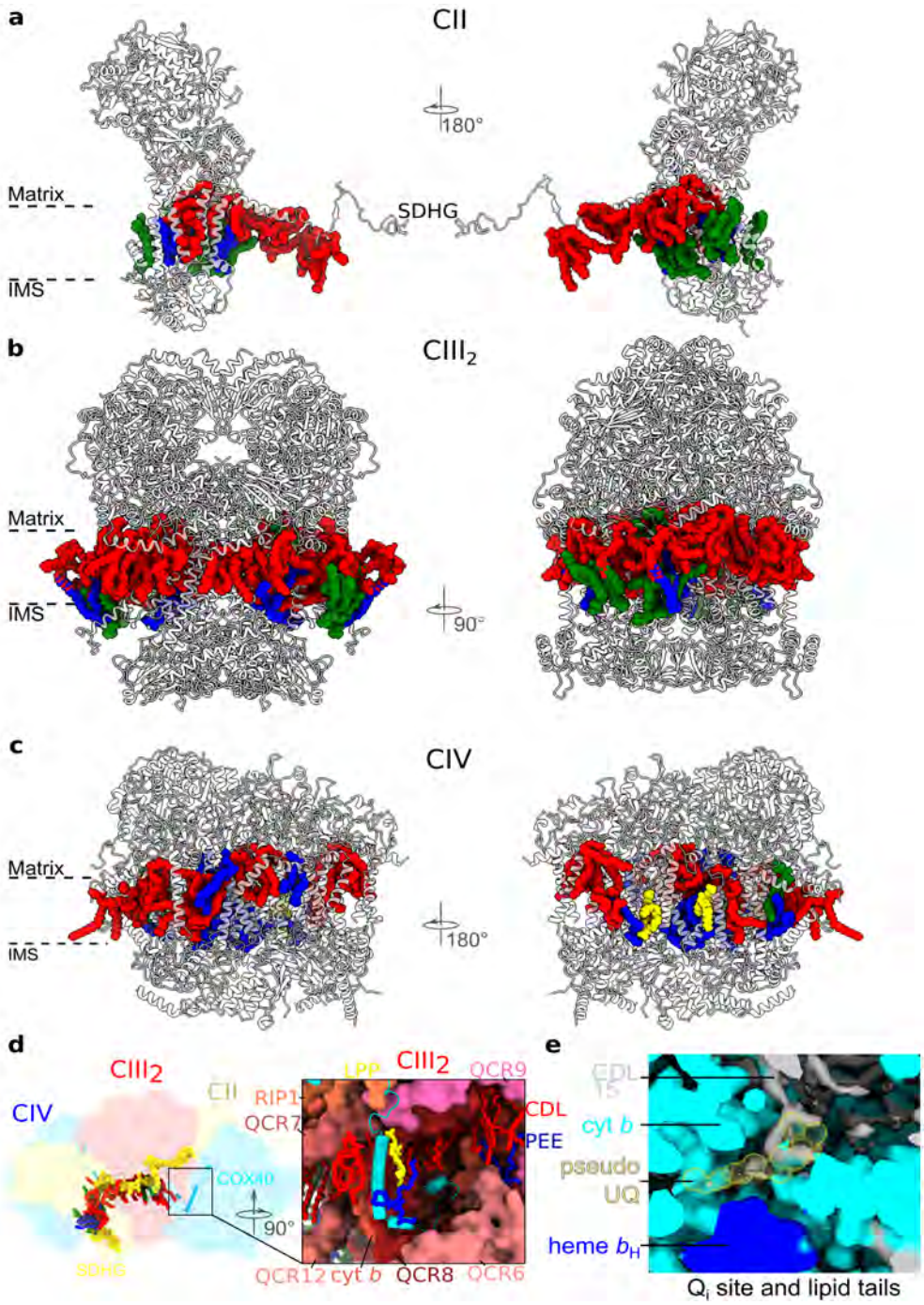

Fig. 4 Bound resolved lipids associated with individual complexes in the supercomplex model. Two side views of CII (**a**), CIII dimer (**b**), CIV (**c**) with bound lipids. Cardiolipin (red), phosphatidylcholine (green) phosphoethanolamine (blue), phosphatidic acid (yellow). **d**, 14 specifically bound lipids to SDHG subunit of CII include 60 cardiolipins, 4 phosphatidylcholines, 32 phosphoethanolamines, 18 phosphatidic acids, which highlight their role in mediating the intercomplex interactions. Close-up view from the CIII-CIV interface further shows COX40 subunit (blue) extending into the CIII cavity (red) filled with specifically bound lipids, namely CDL8 and CDL25. During the motion of CIV related to CIII, lipids provide an environment for the COX40 extension in the cavity. **e**, In the Q_i site of CIII, we didn't observe a UQ density (yellow spheres indicating potential UQ) but we observed the tail of lipid CDL15 extends here.

365 ***COX2* is split into three constituents with reduced hydrophobicity**

366 The high resolution of the data allowed us to detect that the canonical mitochondria-encoded
367 transmembrane CIV subunit 2 (COX2), which acts as the primary electron acceptor from re-
368 duced Cyt *c*, is composed of three separate polypeptides, namely COX2A, COX2B and
369 COX2C. Remarkably, in *P. marinus* all three are encoded in the nucleus (Fig. 5a,b and Fig.
370 S20a). Splitting of functionally important mitochondrial genes was previously reported for
371 soluble subunits in the mitochondrial matrix [36,37], and for *cox2*, splitting into two genes was
372 previously reported for dinoflagellates, alveolates, and chlorophyceae [38]. In our structure,
373 COX2A corresponds to the first N-terminal transmembrane helix of the mammalian counter-
374 part; COX2B corresponds to the second transmembrane helix with 27 amino acids in the IMS
375 that form two antiparallel beta-strands, containing the conserved residues W104 and Q194
376 that stabilise the histidines of the redox-active dinuclear CuA center; COX2C corresponds to
377 the head domain that harbors the active electron acceptor site and complements COX2B with
378 six beta-strands. Since COX2 is directly involved in electron transfer, the assembly of three
379 proteins into the intact unit is a prerequisite for the acceptor site activation. We show that
380 compared to the mammalian mitochondria-encoded COX2, each of the three protein seg-
381 ments in our structure displays a reduced hydrophobicity, resulting in an overall less hydro-
382 phobic protein (Fig. 5b). Therefore, our data supports a potential evolutionary mechanism of
383 membrane subunit splitting end extension that would facilitate gene transfer [39]. Together with
384 our previous observation of a minimal nuclear-encoded subunit-a in the apicomplexan ATP
385 synthase [12], the analysis illustrates how the mitochondrial genome reduction is achieved in
386 evolution through balancing protein hydrophobicity and ensuring the correct localization in
387 the mitochondrial membrane.

388

389 **+2 frameshift occurs in subunits Cyt *b*, COX1 and COX3**

390 The mitochondrial genome of the parasite is extremely reduced, coding for only three protein
391 subunits that are Cyt *b* (CIII), COX1 (CIV) and COX3 (CIV). All three are found in our SC
392 structure. Previous data suggested that COX1-encoding mRNA is not translated in a single
393 reading frame with standard codon usage, but rather shifted ten times at every AGG and CCC
394 codon by one nucleotide (+1) [40]. This phenomenon is termed programmed frameshifting, and
395 it enables expansion of the coding capacity of genomes and the modes through which gene
396 expression can be regulated [41] A structural basis for programmed ribosomal frameshifting of
397 one nucleotide in cytoplasmic translation has been suggested recently [42,43].

398 By comparing the modelled protein residues from our structure with the genomic sequence in
399 the database, we detected eight frameshift events in Cyt *b*, ten in COX1, and one in COX3
400 (Fig. S20b). Intriguingly, three of them appear to represent switching to an alternative read-
401 ing frame that is +2 nucleotides (Fig. 5c) Two are in COX1, at positions P482 and P831, and
402 one in Cyt *b*, at position G38. To date, only an erroneous +2 frameshift has been reported in
403 *Escherichia coli*, which occurs as a result of a translational mistake involving absence of
404 tRNA modification [44] Therefore, our data provide evidence of +2 programmed translational
405 frameshift, and likely occurs on the mitoribosome of the parasite. Our structural data are con-
406 sistent with a recently updated assembly of *Perkinsus* mitochondrial genomes that identified

the frameshift sites across four taxa and suggested a model where it would be driven by tRNA availability resulting in unused codons [45].

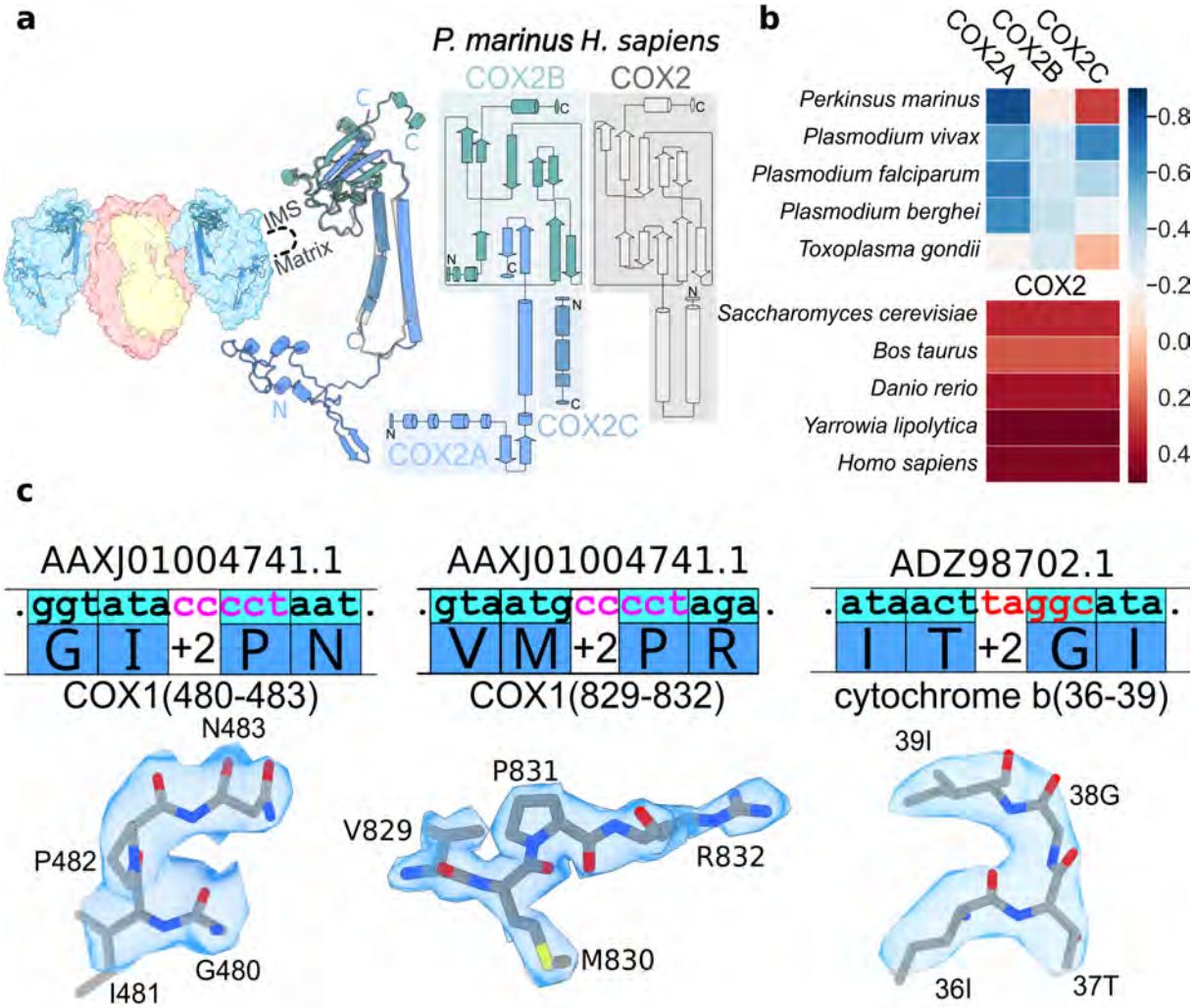

Fig. 5 COX2 protein splitting and COX1, Cyt *b* frameshift phenomenon. a, Comparison of COX2 subunits of *P. marinus* and *H. sapiens* CIV. The superposition demonstrates that functional COX2 in *P. marinus* consists of three separate proteins, namely COX2A (lighter blue), COX2B (green), COX2C (darker blue) encoded in the nucleic genome. The topology diagram comparison shows the organization of the domains that are replaced by three different proteins. COX2B corresponds to the C-terminal domain, whereas a single-helix protein COX2C and one helix from COX2A collectively correspond to the N-terminal domain. **b**, Comparison of relative hydrophobicity of COX2 between apicomplexan parasites, where it is segmented into three nuclear-encoded subunits, and organisms with a single mitochondria-encoded protein. The hydrophobicity is calculated as the grand average of hydropathy according to the Kyte-J.&Doolittle(kd), Moon-Fleming (mf) or Wimley-White (ww). The nuclear-encoded COX2A, 2B and 2C of apicomplexans show a reduced hydrophobicity compared to the canonical protein. **c**, +2 frameshifts in proteins COX1 and Cyt *b* are shown, which have been identified during the model building. Original nucleotide sequence from the database is shown with the amino acids and their corresponding densities that were used to detect the frameshift.

Discussion

Revisiting the 'respirasome' complexity: implications of CII integration

While their role remains to be fully understood, it is clear from previous studies that mitochondrial SCs exhibit compositional and structural plasticity [1,9,46–48]. In ciliates, a stable SC containing all four respiratory chain components was shown to contribute to membrane curvature induction [8]. Notably to date, in organisms lacking CI, only III_2-IV2 or III_2-IV SC structures, incapable of complete electron transport, have been reported [17,18]. CII likely plays a substoichiometric role in optimal electron transfer, and its physical contact with the SC in CI-lacking organisms was not previously structurally implicated. However, inhibitor titration analyses suggested a CII association with CIII and CIV [49], leaving the possibility of direct interaction open.

To elucidate the structural and functional mechanisms of mitochondrial SCs, considering native lipids and unexplored features beyond canonical models, we determined the structure of the SC from the parasite *P. marinus* at 2.12 Å resolution. The SC is coupled to 114 native lipids and 42 co-factors (Fig. 1, Video S1). Our structure revealed two major findings: (1) CII structurally joins the SC, forming a new type of functional II2-III_2-IV2 respirasome allowing complete electron transport from succinate to molecular oxygen; (2) a putative mitochondrial modulator, the ISPR1,2 heterodimer occupies the Cyt *c* binding site on CIII.

CII catalyses the oxidation of succinate to fumarate and increases the electrons available to CIII and CIV via coupled reduction of ubiquinone to ubiquinol in the IMM. Thus, it serves as a link between the tricarboxylic acid cycle and oxidative phosphorylation [50]. In our structure, CII binds to CIII and CIV via specific subunits and lipids. The docking of CII occurs on the matrix side through the apicomplexan subunit SDHG, recognizing the N-terminal extension of CIII subunit QCR7 and extending to CIV subunit COX36. Structural comparisons with yeast [17,18] and plant [19] III-IV SCs shows that CII could occupy the same position as seen in the *P. marinus* SC, with no apparent predictable clashes (Fig. 6), though no proteins have thus far been identified that could mediate such interactions. The contact site between III-IV and CII may be enabled via the unoccupied membrane interface of QCR7 in those species. Thus, this new type of II2-III_2-IV2 respirasome may not be the exclusive feature of the parasite. In a broader perspective, higher-order protein crowding in the membranes of bioenergetic organelles is an emerging pattern elucidated with recent structural studies [1,8,12,51–53]. Our work further demonstrates that the functional arrangement of the respiratory complexes can be more intricate and diverse than previously thought.

A potential regulatory rationale of the II2-III_2-IV2 SC association might be related to the conversion of metabolic reactive oxygen species (ROS). Approximately 90% of the cellular ROS are generated by mitochondria in the form of superoxide O2•−, which is rapidly converted to the more stable H_2O_2 by the enzyme superoxide dismutase (SOD) [54]. CII and CIII are the major sites of ROS generation in mitochondria [55]. In *Mycobacterium smegmatis*, SOD is an integral component of the SCs [56]. In mitochondria, up to 2% of molecular oxygen is reduced to superoxide anions, and if SOD could associate similarly, the presence of CII in the SC implies proximity to SOD, facilitating a more effective defence against oxidative damage due to the abstraction of electrons directly from ROS generators during respiration. Thus, the dense

468 organization of all the respiratory complexes would be beneficial for compartmentalization of
469 the damaging properties.

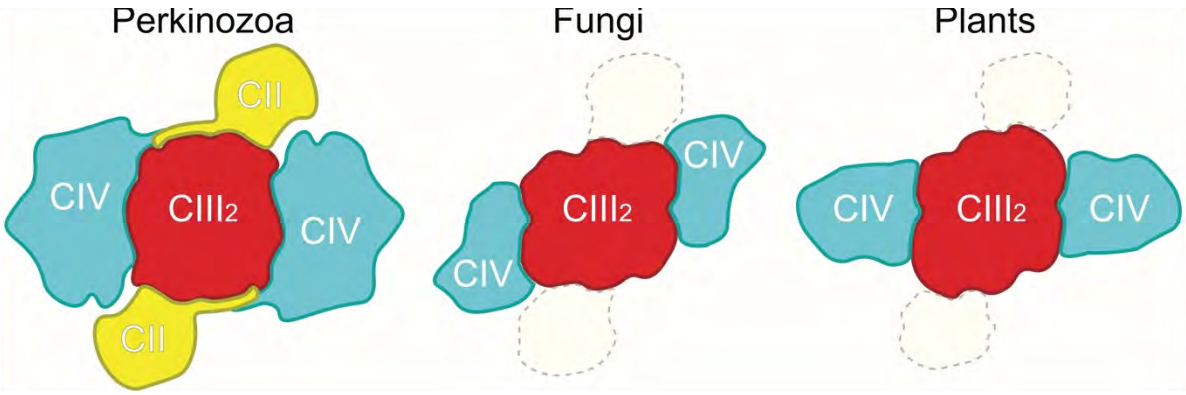

470

471 **Fig. 6 Architecture of II2-III$_2$-IV2 and comparison of CII's relative position at the fungi**
472 **and plant CIII interface.** Left, schematic representation of the *P. marinus*. Middle and right,
473 fungi and plant III-IV, respectively, with their two CIV along the 2-fold axis of CIII$_2$. The
474 relative position of CII (wheat) is outlined with grey dashes, having removed apicomplexan
475 subunits are removed from the interface.

476

477 **ISPR-mediated regulation at the CIII-Cyt *c* interface**

478 The second major finding is that the interactions between CIII and Cyt *c* are modulated in our
479 structure by the presence of the ISPR heterodimer. Co-purification with natural inhibitors is a
480 common theme in the related complex ATP synthase, where its inhibitory factor 1 (IF1) en-
481 ters through the open catalytic interface to mechanistically stall the central stalk rotation and
482 ATP synthesis [12,34,52], which has been proposed to act as a cold-regulated switch [57]. Our find-
483 ing of the ISPR1,2 heterodimer at the highly conserved Cyt *c* binding site suggests that the
484 activity of the SC is also regulated, and CIII is subjected to regulatory signals. Only after
485 ISPR1,2 is removed from CIII, can electron transfer occur (Fig. 7). The deviation from sym-
486 metry between the two proteins maximizes efficiency because the ISPR1 C-terminus has
487 evolved an extension anchoring the heterodimer to CIII, while the ISPR2 N-terminus extends
488 to block the RIP1 head movement that is essential for enzymatic activity. Based on the
489 weaker surface charge of ISPR1,2 compared to Cyt *c* (Fig. S15c), we tested a possible colli-
490 sion-type mechanism for ISPR removal by adding Cyt *c* in excess. However, ISPR1,2 was
491 not outcompeted *in vitro*, suggesting that it is stably bound, and potentially another molecular
492 event might trigger the removal of ISPR1,2 to facilitate enzyme activation and permit elec-
493 tron transfer from CIII to CIV.

494 Biochemical and genetic studies have shown that incorporation of the iron-sulfur protein
495 comes at a late stage of CIII biogenesis [58] and several proteins have been implicated in this
496 maturation process in different species [59-62]. However, only SCAF1, a CIV subunit isoform
497 required for III-IV formation as well as different forms of the CI-containing respirasome in
498 mammals [23,45,63,64] has been shown to remain stably bound to the mature, fully assembled
499 CIII, on the matrix side. No chaperon or assembly factor of CIII is known in Apicomplexa.
500 Interactions of ISPR1,2 with the RIP1 proteins clearly act as a protein inhibitor. Whether it is
501 a regulatory factor or a facilitator of CIII or of the II2-III$_2$-IV2 SC assembly, preventing

premature and potentially damaging electron transfer, remains to be determined. Recently, a negative regulator of CIV has been reported in yeast, namely Mra1 that acts during the assembly of SC [65].

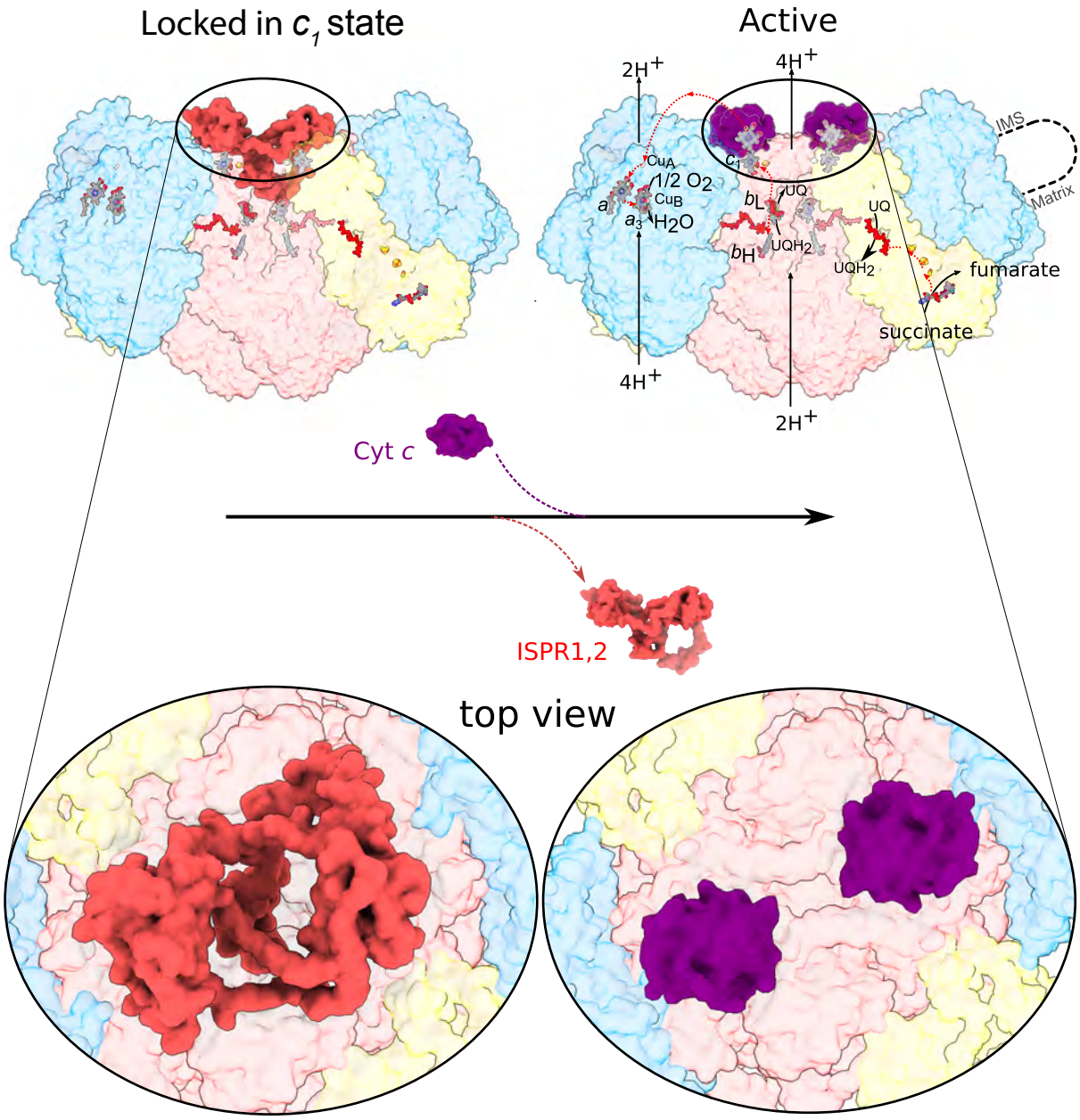

Fig. 7 A model for SC activation. Comparison between ISPR1,2-bound (inactive) and Cyt *c* -bound structures. In the inactive state, ISPR1,2 locks $CIII_2$ in c_1 state. Cofactors of the electron transport chain are shown as stocks and spheres. In the active state, Cyt c_1 occupies the same site (right), that permit electron transfer from CIII to CIV and enzymatic activity of the respirasome.

The role of lipids in SC stability and function

In addition to the identification of new proteins in the SC, the II2-III_2-IV2 model also contains 114 native lipids. This is important because the hierarchical organization of proteins and

515 lipids in the bioenergetic membrane underlies the function of individual respiratory com-
516 plexes and SC formation. To maintain the native lipid composition and determine key mem-
517 brane components and their regulatory properties, we used a gentle solubilization and rapid
518 purification of the material from mitochondria of parasites. The analysis of the lipids reveals
519 their major functions: 1) dynamic interplay with electron carriers in the binding pocket; 2) lu-
520 bricating role for electron carriers; 3) stabilization of intra-complex architecture; 4) contribu-
521 tion to inter-complex association.

522 With regard to the binding pocket of electron carriers, our structure contains a lipid density in
523 the CIII active site. Therefore, the structure suggests that during the electron transfer, lipids
524 and electron carriers continuously replace each other. This is similar to cardiolipin and cho-
525 lesterol found in the c-ring of the ATP synthase from algae [34] and V-ATPase from synaptic
526 vesicles [66], respectively, stalling its rotation, for which a dynamic mechanism has been pro-
527 posed [67].

528 In addition, two structured lipids tightly bound to proteins are found around Q-binding pock-
529 ets. Due to their flexible backbones, those lipids serve as solvents for Q-binding and releas-
530 ing, providing a fluid film lubrication. This affects the chemical composition of the binding
531 pocket and results in a lubricant film. The benefit of the lubrication effect is that it prevents
532 energy losses due to decreased friction during the interfacial motion [68]. Thus, our analysis
533 shows that endogenous lipids have a specific shielding role in reducing activation barriers
534 and accommodating the electron carriers. Active site lipid stabilization was also reported by
535 high-resolution voltage-gated ion channel structures [69], thus it might be a more general phe-
536 nomenon of membrane enzymes.

537 Since the resolution of the density map revealed multiple defined regular densities in the
538 membrane space, it has allowed us to model endogenous lipids that support and stabilize the
539 complex architecture. We illustrate this with the experimental data on CII that differs from
540 the *AlphaFold2* [31] prediction in the transmembrane region, which is the critical part of the
541 model, where some of the helices are displaced. The difference is attributed to the presence of
542 native lipids in our structure that cannot be predicted without experimental data. This exem-
543 plifies the importance of maintaining the lipid native envelop when studying mechanisms of
544 membrane proteins and the limitation of theoretical approaches.

545 Finally, the inter-complex stability in the II2-III_2-IV2 SC is achieved due to the preparation
546 that contains a large fraction of copurified lipids between the complexes. Out of 114 lipids,
547 14 and 13 are located at the II:III and III:IV interfaces, respectively, bridging the SC. This li-
548 pid composition provides a conducive environment for the assembly that can steer the for-
549 mation of the SC, as previously suggested for other SCs [22,70,71]. When the adhesive effect of
550 lipids is maintained, it allows isolation of the higher-order SC, which is consistent with the
551 findings from gram-negative bacteria [72], and bioenergetic complexes from photosynthetic
552 systems [35,73,74]. Thus, our structure shows that the organization of the complete respiratory
553 chain does not only depend on the protein structure but also on the surrounding lipid environ-
554 ment and lipid-protein interactions. This aspect signifies the importance of the native context
555 that must be taken into account when bioenergetic complexes are studied.

556 **Flexibility and evolutionary trends in SC architecture**

557 The lipids surrounding individual complexes at the interfaces likely form a more fluid envi-
558 ronment, fostering relative flexibility between the complexes. Comparative analysis of III-IV
559 interface across fungi, plants, mammals, and ciliates shows species-specific protein composi-
560 tion with no apparent conservation (Fig. S12). This available sampling of structural studies
561 implies a neutral evolution [75] potentially via mechanisms such as growing complexity with
562 protein ratcheting [76], rather than a dispersal evolutionary strategy. Our structural findings sug-
563 gest that in *Perkinsus* due to the additional protein acquisition: 1) no functionally important
564 electrostatic interactions between the positively charged Cyt *c* and the SC are observed [77]; 2)
565 sliding of Cyt *c,* as suggested by NMR studies [78] and kinetic measurements [24], would be fur-
566 ther hindered by the lack of a linear path and the extended distance between the sites (Fig.
567 S15). Thus, a potential compensatory mechanism to address gratuitous protein accumulation
568 is the conformational flexibility revealed by multi-body refinement analysis (Fig. S9). The
569 analysis highlights how structural dynamics of the SC leads to a decrease in the distance be-
570 tween electron donor-acceptor sites, providing an adaptive mechanism to architectural con-
571 straints.

572 Two additional evolutionary aspects of the structure are the splitting of the nucleosomally-
573 encoded COX2 subunit into three complementary segments and programmed +2 frameshifts
574 in subunits Cyt *b* (CIII), COX1 and COX3 (CIV). For each COX2 segment, we observed re-
575 duced hydrophobicity, indicating adaptation for correct localization in the IMM. Expression
576 of the original mitochondrially encoded proteins in the cytoplasm showed a high degradation
577 rate and mistargeting to the endoplasmic reticulum due to recognition by the signal recogni-
578 tion particle [39,79]. Thus, organelle genes encoding hydrophobic proteins are more likely to be
579 retained in the mitochondrial genome. The segmentation of COX2 illustrates how it has
580 evolved under selection for minimizing gene content, allowing its transfer to the nuclear ge-
581 nome without compromising correct localization. Selective constraint on mitochondrial gene
582 expression that modulates its proteins is the coding capacity of the genome, which relies on
583 tRNA availability [45]. In this regard, our structure provides experimental evidence for such a
584 mode of gene expression regulation, where unused codons result in a +2 programmed transla-
585 tional frameshift in the mitochondria of the parasite, consistent with recently reassembled mi-
586 tochondrial genomes of Perkinszoa [45]. Collectively, the evolutionary insights from our struc-
587 ture illustrate how a combination of the adaptive mitochondrial translation system, reduced
588 hydrophobicity of individual gene products, and structural flexibility of the whole SC enable
589 the function of this type of respirasome. Thus, our findings illuminate evolutionary adapta-
590 tions at the gene expression and structural levels as regulatory mechanisms underlying mito-
591 chondrial genome reduction and the growing complexity of proteins in parasites.

592 **Conclusion**

593 In conclusion, this work reveals the II2-III_2-IV2 mitochondrial SC, defines ISPR as a regula-
594 tor of respiration by inhibition of CIII, explains how lipids optimise the function by refining
595 protein structure as well as ligand binding pockets, and proposes evolutionary insight into the
596 modulation of the mitochondrial bioenergetic components. Together, it provides the structural
597 basis for analysis of electron transport regulation and protein evolution in parasitic mitochon-
598 dria.

599 **Methods**

600 Purification of *P. marinus* supercomplex

601 Protistan *P. marinus* was obtained from Kerafast Inc. Cells were grown at 28 °C until an
602 OD_{600} of 0.6 was reached in a medium containing DMEM/F-12 (Sigma D8437), 1.82% sea
603 salt, 0.05% glucose, 0.01% galactose, 0.01% trehalose, 1 mM Gibco GlutaMAX, 0.045 g/L
604 cholesterol, 0.10 g/L cod liver oil fatty acids (methyl esters), 0.25 g/L polyoxyethylenesorbi-
605 tan monooleate, 0.20 g/L D-α-tocopherol acetate, 2% fetal bovine serum [80]. 14 L of media
606 produced ~42 gr of cell pellet. Cell pellets were washed in homogenization buffer containing
607 20 mM HEPES-KOH pH 7.5, 350 mM mannitol, 5 mM EDTA and lysed with glass beads
608 (500 µm) using the FastPrep-24™ 5G Beadbeater at 6 meter/sec for 25 sec in a cold room.
609 The lysis was assessed by a light microscope until ~ 70% breakage was achieved. All the
610 consequent steps were performed in 4 ^{0}C or on ice. Cell debris and nuclei were separated
611 through centrifugation at 1200 x *g* for 15 min. Mitochondria were isolated by centrifugation
612 at 10,000 x *g* for 15 min, followed by a sucrose gradient with 15%, 23%, 32%, 60% w/v su-
613 crose in buffer containing 20 mM HEPES KOH pH 7.5, 1 mM EDTA at 14,000 g for 60 min
614 in SW40 rotor. Mitochondria were lysed in a buffer containing 25mM HEPES-KOH (pH
615 7.5), 50 mM KCl, 20mM $Mg(CH3COO)_2$, 2% digitonin, 250 µL RNAase inhibitors, protease
616 inhibitors and incubated for 30 min. The membranes were then separated by centrifugation at
617 30,000 x *g* for 20 min, and the supernatant was loaded on a 1 M sucrose cushion in a buffer
618 containing 25 mM HEPES-KOH pH 7.5, 50 mM KCl, 20 mM $Mg(CH3COO)_2$, 0.1 % digi-
619 tonin and centrifuged at 164244 x *g* (40000 rpm) for 3 h in Ti70 rotor. Resuspended pellets
620 were cleared by centrifugation at 30,000 x *g* for 20 min and loaded on a Superose 6 Increase
621 3.2/300 column. Eluted peak fractions were used immediately for cryo-grid preparation.

622 Cryo-EM sample preparation, data collection and image processing

623 Quantifoil R2/2-300 grids floated with a homemade 3-nm amorphous carbon layer were
624 glow-discharged before applying a 3 µl sample and vitrified in a Vitrobot Mark IV, with a 30-
625 sec waiting time before blotting grids for 3 sec. Three data sets of a total of 43,464 movies
626 were collected on a Titan Krios electron microscope (Thermo Fisher Scientific) operated at
627 300 kV using automated single-particle acquisition software (EPU) with a K3 detector at a
628 pixel size of 0.51 Å, 0.86 Å, 0.51 Å. Data statistics are shown in Tables S1 and S2.

629 Movie stacks were motion corrected and dose weighted using MotionCor2 [81]. Contrast trans-
630 fer function (CTF) of the motion-corrected micrographs was estimated using Gctf [82]. Micro-
631 graphs were grouped based on optic difference, beam shift in X and Y axis using custom py-
632 thon scripts. ~2,620,000 particles were picked using Gautomatch [83] and coordinates were im-
633 ported into RELION 3.1 [84]. Particles were extracted in a unified pixel size 0.86 Å during
634 Bayesian polishing in RELION 3.1 [84], then all particles were combined and refined together.
635 The particles were subjected to 3D classification using references generated by an initial
636 model to separate supercomplex particles from copurified ATP synthase. The particles of su-
637 percomplex were subjected to auto-refinement to improve the angular assignments with a sol-
638 vent mask applied. The obtained 3D reconstructions were used as a reference for CTF refine-
639 ment. Bayesian polishing was performed, followed by another round of CTF refinement. The
640 resulting 524,289 particles were used for auto-refinement. Masked refinements of the

respective supercomplex subregions resulted in map resolutions of 2.12 Å for the entire supercomplex applying C2 symmetry, 2.16 Å for CII head, 2.17 Å for CIV, and 2.06 Å for CII2CIII$_2$. Local resolution was estimated by RELION [85,86]. The workflow is further illustrated in Fig. S2d.

Signal subtraction of CIV followed by CII2CIII$_2$ refinement with a local angle search was perfomed. Focused classification using a mask around two Rieske protein was performed. The c_1-state (111,717 particles), *b*-state (47,561 particles), and intermediate state (137,612 particles) were obtained. For c_1 state, we further classified into two classes that are symmetry related to each other. Particles from class 2 were expanded with C2 symmetry and the unrotated particles in the expanded star file were removed to only keep one copy (class 1). Then particles of class 1 and rotated class 2 were combined and recovered back to the original particles with CIV signal and locally refined to 2.47 Å. For *b*-state and intermediate, their particles were recovered back to the original particles separately and locally refined to 2.42 Å and 2.18 Å with C2 symmetry. The results are shown in Fig. S3b.

Model building and refinement

Models for specific proteins (Fig. S7) were built *de novo*, starting with polyalanine traces built manually in *Coot* [28]. These initial traces were then used as templates to assign side chains or secondary structure. Protein were idnetified by comparing the assigned sequence against proteome databases. Chains 3G (g), 4Q (q), 40 (1), 2U (u), 3K (k), 30 (1) were identified using open reading frames. Detection of bulky residues W, Y, and C-C motifs was used to simplify the search space. The corresponding genes coding for those chains were eventually found in the whole genome shotgun sequences scf_110429693096, AAXJ01004741.1, AAXJ01002945.1, AAXJ01000691.1, AAXJ01000150.1, scf_1104296932410 1 749426 1 and scf_1104296971434 1 346455 1, respectively.

For chains 3G(g), 4Q(q), and 40(1), tracing sequences did not fit the density, and we manually applied frameshifts +1 or +2 to correctly fit amino acid identities to the map. Thus, all frameshifts were found independently and without using any additional information. The detected frameshifts of mitochondrial proteins COX1, COX3, and Cyt *b* with their corresponding nucleotide and protein sequences are summarized in Fig. S20, and densities for +2 frameshift events are shown in Fig. 5.

For protein sequences of chain 3L(l), we considered two hits: C5KXQ7 and C5LDF5 from protein database. C5LDF5, Aurora kinase, contains the reading frame of C5KXQ7. However, no unique peptides for C5LDF5 were identified by our mass-spectrometry analysis (see source file), thus the longer protein version has been excluded, and we assigned 3L(l) as C5KXQ7. For chain 2U, the last two residues A and M from the reading frame can't fit the density, though the rest of residues from the translation of AAXJ01000691.1 fit the density well. Sequencing mistakes cannot be excluded.

The three states of Rieske protein head were built based in their related state maps. The lipids and digitonin were especially restrained by the cif files generated from Grade Web Server (http://grade.globalphasing.org/). Other ligands that are not in the default library were generated by eLbow in Phenix [87]. Here, the 'edit' file that defines metal-coordination bonds was generated either by ReadySet in the Phenix suite or manually. Final models were further

683 subjected to refinement with Phenix real_space_refinement v1.19.2-000 [87], wherein, five
684 macro-cycles of global energy minimization with 'edit', secondary structure restraints, and
685 rotamer restraints.

686 After one monomer was properly refined, the C2 symmetric monomer was generated from
687 the model and the two were combined. Conflicting residues between two monomers were re-
688 built in *Coot* [28] manually. The full model then was refined again in Phenix [87] with reference
689 model restraints. The model of masked parts, CII head, CIV, and $CII2CIII_2$ were extracted
690 from the full model and refined again using related half-maps in Phenix [87].

691 Cyt c_1-Cyt *c* complex in Fig. 3a was modelled with *AlphaFold2* [31]. *Perkinsus* CII transmem-
692 brane region shown in Fig. S19 was predicted using the modified Python notebook Al-
693 phaFold2_advanced.ipynb (https://colab.research.google.com/github/sokrypton/Colab-
694 Fold/blob/main/beta/AlphaFold2_advanced.ipynb) from ColabFold [88] on a local computer in-
695 dependent of Google Colab, where homooligomer, msa_method, and used_amber_relax are
696 set as 1, jackhammer, and True, respectively. The following protein IDs have been used for
697 *AlphaFold2* [31] modeling:

2O/2o	SDHG	XP_002780482.1	C5KTH2
2P/2p	SDHF	XP_002767545.1	C5LSM2
2Q/2q	SDHD	XP_002787086	C5K9W0
2R/2r	SDHH	AAXJ01000252.1 (contig)	/
2S/2s	SDHE	XP_002777439.1	C5L1Y6
2T/2t	SDHJ	XP_002783522.1	C5KJI4
2U/2u	SDHC	AAXJ01000691.1 (contig)	/
2V/2v	SDHI	XP_002773883.1	C5LCL6

698 The refinement and validation statistics are presented in Tables S1 and S2. Multiple rounds of
699 validation and model building were carried out using MolProbity and *Coot* [28]. For further val-
700 idation, the PDB Validation server was used (https://validate-rcsb-2.wwpdb.org). The struc-
701 ture was analysed using *Coot* [28] and *ChimeraX* [89]. Figures were prepared in ChimeraX [89] with
702 additional graphical elements created using Inkscape.

703 Mass spectrometry

704 The purified samples were lysed by 4 % SDS lysis buffer and prepared for mass spectrometry
705 analysis using a modified version of the SP3 protein clean up and digestion protocol [90]. 33
706 and 22 µg protein were alkylated with 4 mM Chloroacetamide. Sera-Mag SP3 bead mix (20
707 µl) was transferred into the protein sample together with 100% Acetonitrile to a final concen-
708 tration of 70 %. The mix was incubated under rotation at room temperature for 18 min. The
709 mix was placed on the magnetic rack and the supernatant was discarded, followed by two
710 washes with 70 % ethanol and one with 100 % acetonitrile. The beads-protein mixture was
711 reconstituted in 100 µl LysC buffer (0.5 M Urea, 50 mM HEPES pH: 7.6 and 1:50 enzyme
712 (Trypsin) to protein ratio) and incubated overnight. Finally, the peptide samples were de-
713 salted by SCX clean up. The final peptide concentration was determined by the Bio-Rad DC

714 Assay.An aliquot of approximately 10 µg was suspended in LC mobile phase A and 2 µg was
715 injected on the LC-MS/MS system.

716 Online LC-MS was performed using a Dionex UltiMate™ 3000 RSLCnano System coupled
717 to a Q-Exactive High Field mass spectrometer (Thermo Scientific). 3 uL was injected from
718 each sample. Samples were trapped on a C_18 guard desalting column (Acclaim PepMap 100,
719 75 µm x 2 cm, nanoViper, C_18, 5 µm, 100 Å), and separated on a 50 cm long C_18 column
720 (Easy spray PepMap RSLC, C_18, 2 µm, 100Å, 75 µmx50cm). The nano capillary solvent A
721 was 95% water, 5%DMSO, 0.1% formic acid; and solvent B was 5% water, 5% DMSO, 95%
722 acetonitrile, 0.1% formic acid. At a constant flow of 0.25 µl min^{-1}, the curved gradient went
723 from 6%B up to 43%B in 180 min, followed by a steep increase to 100%B in 5 min.

724 FTMS master scans with 60,000 resolution (and mass range 300-1500 m/z) were followed by
725 data-dependent MS/MS (30 000 resolution) on the top 5 ions using higher energy collision
726 dissociation (HCD) at 30% normalized collision energy. Precursors were isolated with a
727 1,2m/z window. Automatic gain control (AGC) targets were 1e6 for MS1 and 1e5 for MS2.
728 Maximum injection times were 100 msec for MS1 and MS2. The entire duty cycle lasted
729 ~2.5 sec. Dynamic exclusion was used with 60 sec duration. Precursors with unassigned
730 charge state or charge state 1 were excluded. An underfill ratio of 1% was used.

731 The MS raw files were searched using Sequest-Percolator or Target Decoy PSM Validator
732 under the software platform Proteome Discoverer 1.4 (Thermo Scientific) against *P. marinus*
733 (strain ATCC 50983) Uniprot database and filtered to a 1% FDR cut off.

734 We used a precursor ion mass tolerance of 10 ppm, and production mass tolerances of 0.02
735 Da for HCD-FTMS. The algorithm considered tryptic peptides with a maximum of 2 missed
736 cleavage; carbamidomethylation (C) as fixed modification and oxidation (M) as variable
737 modifications.

738 <u>Gel Electrophoresis, protein staining and in gel-activity assay</u>

739 Pre-cast gels (NativePAGE™ 3 to 12%, BIS-TRIS, 1.0 mm, Mini Protein Gel, Invitrogen)
740 were used for Clear Native (CN) PAGE with two identical sample lanes of the purified super-
741 complex sample post sucrose cushion and a protein ladder lane (NativeMark™, Invitrogen),
742 prepared according to the manufacturer's instructions. The gel electrophoresis was conducted
743 at 4°C, firstly at 150 V for 30 min with NativePage Light Blue Cathode buffer and then at
744 250 V for 150 min with NativePAGE Anode Buffer. The two sample lanes were then cut.
745 One was stained with Coomassie Brilliant Blue overnight and then destained with an etha-
746 nol/acetic acid solution. The other sample lane was incubated for 45 min in a solution of 50
747 mM KPi pH 7.4 containing 0.5 mg/mL 3,3′-diaminobenzidine (DAB) and 1 mg/mL equine
748 cytochrome *c* before incubation in 10 % acetic acid.

749 <u>Activity measurements</u>

750 The functional integrity of the SC was assessed polarographically using an oxygen electrode
751 (Oxygraph+ system, Hansatech Instruments). All measurements were carried out at 25°C in a
752 solution of 10 mM KPi, 50 mM KCl at pH 6.6 supplemented with 500 units/mL superoxide
753 dismutase, 250 units/mL catalase and 0.05% digitonin. A typical experiment started with ad-
754 dition of 20-30 nM SC and the rate left to stabilise before addition of 10 mM Na^+-succinate
755 (substrate of CII) followed by 50 µM equine cytochrome *c*. The CII-to-CIV reaction was

stopped with addition of 10 mM Na^+-malonate (inhibitor of CII). Subsequently, 40 µM decylubiquinol (substrate of CIII) was added before the CIII-to-CIV reaction was stopped with addition of 10 µM antimycin A (inhibitor of CIII). Finally, 2 mM Na^+-ascorbate and 40 µM TMPD were added and the CIV reaction thereafter stopped with addition of 1 mM KCN. The reaction vessel was washed with a solution containing BSA in between experiments to remove any residual of inhibitors.

Reaction rates were derived from the oxygen consumption rate recorded after addition of each specific substrate using the final KCN-inhibited rate as a baseline. Conversion to turnover numbers was made using the concentration of CIV in the sample, assuming that in the purified SC sample, all the CIV is in the SC, as supported by in-gel activity performed on CN-PAGE gel. CIV concentration was determined from a dithionite-reduced *minus* oxidised difference visible spectrum recorded in 25mM HEPES, 25 mM KCl, 5 mM $MgCl_2$ and 0.1% digitonin at pH 7.5 using the specific difference in absorption associated to the reduction of the A-type hemes of CIV (ΔA 603-621 nm, extinction coefficient of 26,000 $M^{-1}cm^{-1}$).

Data availability statement

The atomic coordinates were deposited in the Protein Data Bank (PDB) under accession numbers XXXX (c_1 state), XXXX (*b* state), XXXX (intermediate). The cryo-EM maps have been deposited in the Electron Microscopy Data Bank (EMDB) under the respective accession numbers: EMD-1XXXX c_1 state combined map), EMD-1XXXX(*b* state combined map), EMD-1XXXX (intermediate combined map), EMD-1XXXX (c_1 state CII_2CIII2), EMD-1XXXX (*b* sate $CII2CIII_2$), EMD-1XXXX (intermediate CII2CIII2), EMD-50354 (concensus $II2III_2IV2$), EMD-1XXXX (CII head), and EMD-1XXXX (CIV) and EMD-1XXXX ($CII2CIII_2$). An Excel file containing the visible absorption spectroscopy data and their analysis has been added. All the data will be publicly available. Source data are provided with this paper.

References

1. Zheng, W., Chai, P., Zhu, J. & Zhang, K. High-resolution In-situ Structures of Mammalian Mitochondrial Respiratory Supercomplexes in Reaction within Native Mitochondria. Preprint at https://doi.org/10.1101/2024.04.02.587796 (2024).
2. Greggio, C. *et al.* Enhanced Respiratory Chain Supercomplex Formation in Response to Exercise in Human Skeletal Muscle. *Cell Metab.* **25**, 301–311 (2017).
3. Gonzalez-Franquesa, A. *et al.* Mass-spectrometry-based proteomics reveals mitochondrial supercomplexome plasticity. *Cell Rep.* **35**, 109180 (2021).
4. Hollinshead, K. E. R. *et al.* Respiratory Supercomplexes Promote Mitochondrial Efficiency and Growth in Severely Hypoxic Pancreatic Cancer. *Cell Rep.* **33**, 108231 (2020).

5. Wang, G., Popovic, B., Tao, J. & Jiang, A. Overexpression of COX7RP promotes tumor growth and metastasis by inducing ROS production in hepatocellular carcinoma cells. *Am. J. Cancer Res.* **10**, 1366–1383 (2020).
6. Zheng, Y., Gibb, A. A., Xu, H., Liu, S. & Hill, B. G. The metabolic state of the heart regulates mitochondrial supercomplex abundance in mice. *Redox Biol.* **63**, 102740 (2023).
7. Han, F. *et al.* Structures of Tetrahymena thermophila respiratory megacomplexes on the tubular mitochondrial cristae. *Nat. Commun.* **14**, 2542 (2023).
8. Mühleip, A. *et al.* Structural basis of mitochondrial membrane bending by the I–II–III2–IV2 supercomplex. *Nature* **615**, 934–938 (2023).
9. Zhang, L. *et al.* Structural basis for the regulatory mechanism of mammalian mitochondrial respiratory chain megacomplex-I2III2IV2. *hLife* **2**, 189–200 (2024).
10. Flegontov, P. *et al.* Divergent mitochondrial respiratory chains in phototrophic relatives of apicomplexan parasites. *Mol. Biol. Evol.* **32**, 1115–1131 (2015).
11. Roger, A. J., Muñoz-Gómez, S. A. & Kamikawa, R. The Origin and Diversification of Mitochondria. *Curr. Biol. CB* **27**, R1177–R1192 (2017).
12. Mühleip, A., Flygaard, R. K., Ovciarikova, J. & Amunts, A. ATP synthase hexamer assemblies shape cristae of Toxoplasma mitochondria. *Nat. Commun.* (2021).
13. Evers, F. *et al.* Composition and stage dynamics of mitochondrial complexes in Plasmodium falciparum. *bioRxiv* 2020.10.05.326496 (2020) doi:10.1101/2020.10.05.326496.
14. Maclean, A. E. *et al.* Complexome profile of Toxoplasma gondii mitochondria identifies divergent subunits of respiratory chain complexes including new subunits of cytochrome bc1 complex. *PLOS Pathog.* **17**, e1009301 (2021).
15. Einarsson, E. *et al.* Development of the Myzozoan Aquatic Parasite Perkinsus marinus as A Versatile Experimental Genetic Model Organism. *Protist* **172**, 125830 (2021).
16. Zhang, Z. *et al.* Electron transfer by domain movement in cytochrome bc 1. *Nature* **392**, 677–684 (1998).
17. Hartley, A. M. *et al.* Structure of yeast cytochrome c oxidase in a supercomplex with cytochrome bc1. *Nat. Struct. Mol. Biol.* **26**, 78–83 (2019).

18. Rathore, S. *et al.* Cryo-EM structure of the yeast respiratory supercomplex. *Nat. Struct. Mol. Biol.* **26**, 50–57 (2019).
19. Maldonado, M., Guo, F. & Letts, J. A. Atomic structures of respiratory complex III2, complex IV, and supercomplex III2-IV from vascular plants. *eLife* (2021) doi:10.7554/eLife.62047.
20. Hartley, A. M., Meunier, B., Pinotsis, N. & Maréchal, A. Rcf2 revealed in cryo-EM structures of hypoxic isoforms of mature mitochondrial III-IV supercomplexes. *Proc. Natl. Acad. Sci.* **117**, 9329–9337 (2020).
21. Moe, A., Dimogkioka, A.-R., Rapaport, D., Öjemyr, L. N. & Brzezinski, P. Structure and function of the S. pombe III-IV-cyt c supercomplex. *Proc. Natl. Acad. Sci. U. S. A.* **120**, e2307697120 (2023).
22. Guo, R., Zong, S., Wu, M., Gu, J. & Yang, M. Architecture of Human Mitochondrial Respiratory Megacomplex I2III2IV2. *Cell* **170**, 1247-1257.e12 (2017).
23. Vercellino, I. & Sazanov, L. A. Structure and assembly of the mammalian mitochondrial supercomplex CIII2CIV. *Nature* **598**, 364–367 (2021).
24. Moe, A., Trani, J. D., Rubinstein, J. L. & Brzezinski, P. Cryo-EM structure and kinetics reveal electron transfer by 2D diffusion of cytochrome c in the yeast III-IV respiratory supercomplex. *Proc. Natl. Acad. Sci.* **118**, (2021).
25. Fernández-Vizarra, E. & Zeviani, M. Nuclear gene mutations as the cause of mitochondrial complex III deficiency. *Front. Genet.* **6**, 134 (2015).
26. Fernandez-Vizarra, E. & Zeviani, M. Mitochondrial complex III Rieske Fe-S protein processing and assembly. *Cell Cycle Georget. Tex* **17**, 681–687 (2018).
27. Emsley, P. & Cowtan, K. Coot: model-building tools for molecular graphics. *Acta Crystallogr. D Biol. Crystallogr.* **60**, 2126–2132 (2004).
28. Emsley, P., Lohkamp, B., Scott, W. G. & Cowtan, K. Features and development of *Coot*. *Acta Crystallogr. D Biol. Crystallogr.* **66**, 486–501 (2010).
29. Sayers, E. W. *et al.* Database resources of the National Center for Biotechnology Information. *Nucleic Acids Res.* **50**, D20–D26 (2021).

30. Berná, L. *et al.* Reevaluation of the Toxoplasma gondii and Neospora caninum genomes reveals misassembly, karyotype differences, and chromosomal rearrangements. *Genome Res.* **31**, 823–833 (2021).
31. Jumper, J. *et al.* Highly accurate protein structure prediction with AlphaFold. *Nature* **596**, 583–589 (2021).
32. Bennett, C. F. *et al.* Peroxisomal-derived ether phospholipids link nucleotides to respirasome assembly. *Nat. Chem. Biol.* **17**, 703–710 (2021).
33. Kagan, V. E. *et al.* Cytochrome c/cardiolipin relations in mitochondria: a kiss of death. *Free Radic. Biol. Med.* **46**, 1439–1453 (2009).
34. Mühleip, A., McComas, S. E. & Amunts, A. Structure of a mitochondrial ATP synthase with bound native cardiolipin. *eLife* **8**, e51179 (2019).
35. Chen, M. *et al.* Distinct structural modulation of photosystem I and lipid environment stabilizes its tetrameric assembly. *Nat. Plants* **6**, 314–320 (2020).
36. Tobiasson, V. & Amunts, A. Ciliate mitoribosome illuminates evolutionary steps of mitochondrial translation. *eLife* **9**, e59264 (2020).
37. Soufari, H. *et al.* Structure of the full kinetoplastids mitoribosome and insight on its large subunit maturation. *bioRxiv* 2020.05.02.073890 (2020) doi:10.1101/2020.05.02.073890.
38. Waller, R. F. & Keeling, P. J. Alveolate and chlorophycean mitochondrial *cox2* genes split twice independently. *Gene* **383**, 33–37 (2006).
39. Björkholm, P., Harish, A., Hagström, E., Ernst, A. M. & Andersson, S. G. E. Mitochondrial genomes are retained by selective constraints on protein targeting. *Proc. Natl. Acad. Sci.* **112**, 10154–10161 (2015).
40. Masuda, I., Matsuzaki, M. & Kita, K. Extensive frameshift at all AGG and CCC codons in the mitochondrial cytochrome c oxidase subunit 1 gene of Perkinsus marinus (Alveolata; Dinoflagellata). *Nucleic Acids Res.* **38**, 6186–6194 (2010).
41. Dinman, J. D. Control of gene expression by translational recoding. *Adv. Protein Chem. Struct. Biol.* **86**, 129–149 (2012).
42. Demo, G. *et al.* Structural basis for +1 ribosomal frameshifting during EF-G-catalyzed translocation. *Nat. Commun.* **12**, 4644 (2021).

43. Bhatt, P. R. *et al.* Structural basis of ribosomal frameshifting during translation of the SARS-CoV-2 RNA genome. *bioRxiv* 2020.10.26.355099 (2020) doi:10.1101/2020.10.26.355099.
44. Brégeon, D., Colot, V., Radman, M. & Taddei, F. Translational misreading: a tRNA modification counteracts a +2 ribosomal frameshift. *Genes Dev.* **15**, 2295–2306 (2001).
45. Gornik, S. G. *et al.* Mitochondrial Genomes in Perkinsus Decode Conserved Frameshifts in All Genes. *Mol. Biol. Evol.* **39**, msac191 (2022).
46. Vercellino, I. & Sazanov, L. A. SCAF1 drives the compositional diversity of mammalian respirasomes. *Nat. Struct. Mol. Biol.* 1–11 (2024) doi:10.1038/s41594-024-01255-0.
47. Klusch, N. *et al.* Cryo-EM structure of the respiratory I + III2 supercomplex from Arabidopsis thaliana at 2 Å resolution. *Nat. Plants* **9**, 142–156 (2023).
48. He, Z. *et al.* Euglena's atypical respiratory chain adapts to the discoidal cristae and flexible metabolism. *Nat. Commun.* **15**, 1628 (2024).
49. Boumans, H., Grivell, L. A. & Berden, J. A. The respiratory chain in yeast behaves as a single functional unit. *J. Biol. Chem.* **273**, 4872–4877 (1998).
50. Bezawork-Geleta, A., Rohlena, J., Dong, L., Pacak, K. & Neuzil, J. Mitochondrial Complex II: At the Crossroads. *Trends Biochem. Sci.* **42**, 312–325 (2017).
51. You, X. *et al.* In situ structure of the red algal phycobilisome-PSII-PSI-LHC megacomplex. *Nature* **616**, 199–206 (2023).
52. Flygaard, R. K., Mühleip, A., Tobiasson, V. & Amunts, A. Type III ATP synthase is a symmetry-deviated dimer that induces membrane curvature through tetramerization. *Nat. Commun.* **11**, 5342 (2020).
53. Naschberger, A. *et al.* Algal photosystem I dimer and high-resolution model of PSI-plastocyanin complex. *Nat. Plants* **8**, 1191–1201 (2022).
54. Balaban, R. S., Nemoto, S. & Finkel, T. Mitochondria, oxidants, and aging. *Cell* **120**, 483–495 (2005).
55. Hadrava Vanova, K., Kraus, M., Neuzil, J. & Rohlena, J. Mitochondrial complex II and reactive oxygen species in disease and therapy. *Redox Rep. Commun. Free Radic. Res.* **25**, 26–32 (2020).

56. Gong, H. *et al.* An electron transfer path connects subunits of a mycobacterial respiratory supercomplex. *Science* **362**, eaat8923 (2018).
57. Bartelt, A. IF1 controls UCP1-dependent mitochondrial bioenergetics in brown adipocytes. (2023).
58. Zara, V., Conte, L. & Trumpower, B. L. Evidence that the assembly of the yeast cytochrome bc1 complex involves the formation of a large core structure in the inner mitochondrial membrane. *the FEBS Journal* **276**, 1900–1914 (2009).
59. Sánchez, E. *et al.* LYRM7/MZM1L is a UQCRFS1 chaperone involved in the last steps of mitochondrial Complex III assembly in human cells. *Biochimica Et Biophysica Acta. Bioenergetics* **1827**, 285–293 (2013).
60. Hevler, J. F. *et al.* Molecular characterization of a complex of apoptosis-inducing factor 1 with cytochrome c oxidase of the mitochondrial respiratory chain. *Proc. Natl. Acad. Sci.* **118**, e2106950118 (2021).
61. Signes, A. & Fernandez-Vizarra, E. Assembly of mammalian oxidative phosphorylation complexes I-V and supercomplexes. *Essays Biochem.* **62**, 255–270 (2018).
62. Cruciat, C., Hell, K., Fölsch, H., Neupert, W. & Stuart, R. A. Bcs1p, an AAA-family member, is a chaperone for the assembly of the cytochrome bc1 complex. *EMBO J.* **18**, 5226–5233 (1999).
63. Fernandez-Vizarra, E. *et al.* Impaired complex III assembly associated with BCS1L gene mutations in isolated mitochondrial encephalopathy. *Hum. Mol. Genet.* **16**, 1241–1252 (2007).
64. Fernández-Vizarra, E. *et al.* Two independent respiratory chains adapt OXPHOS performance to glycolytic switch. *Cell Metabolism* **34**, 1792-1808.e6 (2022).
65. Moretti-Horten, D. N. *et al.* Synchronized assembly of the oxidative phosphorylation system controls mitochondrial respiration in yeast. *Dev. Cell* **59**, 1043-1057.e8 (2024).
66. Coupland, C. E. *et al.* High resolution cryo-EM of V-ATPase in native synaptic vesicles. Preprint at https://doi.org/10.1101/2024.04.01.587493 (2024).

67. Duncan, A. L., Robinson, A. J. & Walker, J. E. Cardiolipin binds selectively but transiently to conserved lysine residues in the rotor of metazoan ATP synthases. *Proc. Natl. Acad. Sci.* **113**, 8687–8692 (2016).
68. Almendro-Vedia, V. *et al.* How rotating ATP synthases can modulate membrane structure. *Arch. Biochem. Biophys.* **708**, 108939 (2021).
69. Huang, J. *et al.* Structural basis for human Cav3.2 inhibition by selective antagonists. *Cell Res.* 1–11 (2024) doi:10.1038/s41422-024-00959-8.
70. Ing, G., Hartley, A. M., Pinotsis, N. & Maréchal, A. Cryo-EM structure of a monomeric yeast S. cerevisiae complex IV isolated with maltosides: Implications in supercomplex formation. *Biochim. Biophys. Acta Bioenerg.* **1863**, 148591 (2022).
71. Hryc, C. F. *et al.* Structural insights into cardiolipin replacement by phosphatidylglycerol in a cardiolipin-lacking yeast respiratory supercomplex. *Nat. Commun.* **14**, 2783 (2023).
72. Webby, M. N. *et al.* Lipids mediate supramolecular outer membrane protein assembly in bacteria. *Sci. Adv.* **8**, eadc9566 (2022).
73. Pan, X. *et al.* Structural basis of LhcbM5-mediated state transitions in green algae. *Nat. Plants* **7**, 1119–1131 (2021).
74. Kühlbrandt, W. The Resolution Revolution. *Science* **343**, 1443–1444 (2014).
75. Lukeš, J., Archibald, J. M., Keeling, P. J., Doolittle, W. F. & Gray, M. W. How a neutral evolutionary ratchet can build cellular complexity. *IUBMB Life* **63**, 528–537 (2011).
76. Hochberg, G. K. A. *et al.* A hydrophobic ratchet entrenches molecular complexes. *Nature* **588**, 503–508 (2020).
77. Trouillard, M., Meunier, B. & Rappaport, F. Questioning the functional relevance of mitochondrial supercomplexes by time-resolved analysis of the respiratory chain. *Proc. Natl. Acad. Sci.* **108**, E1027–E1034 (2011).
78. Moreno-Beltrán, B. *et al.* Respiratory complexes III and IV can each bind two molecules of cytochrome c at low ionic strength. *FEBS Lett.* **589**, 476–483 (2015).
79. Adams, K. L. & Palmer, J. D. Evolution of mitochondrial gene content: gene loss and transfer to the nucleus. *Mol. Phylogenet. Evol.* **29**, 380–395 (2003).

80. Gauthier, J. D. & Vasta, G. R. In Vitro Culture of the Eastern Oyster Parasite Perkinsus marinus: Optimization of the Methodology. *J. Invertebr. Pathol.* **66**, 156–168 (1995).

81. Zheng, Shawn Q., Eugene Palovcak, Jean-Paul Armache, Kliment A. Verba, Yifan Cheng, and David A. Agard. 2017. "MotionCor2: Anisotropic Correction of Beam-Induced Motion for Improved Cryo-Electron Microscopy." *Nature Methods* 14 (4): 331–32.

82. Zhang, K. Gctf: Real-time CTF determination and correction. *J. Struct. Biol.* **193**, 1–12 (2016).

83. Developed by K. Zhang, MRC Laboratory of Molecular Biology, Cambridge, UK. http://www.mrc-lmb.cam.ac.uk/kzhang/Gautomatch

84. Zivanov, J. *et al.* New tools for automated high-resolution cryo-EM structure determination in RELION-3. *eLife* **7**, e42166 (2018).

85. Scheres, S. H. W. RELION: Implementation of a Bayesian approach to cryo-EM structure determination. *J. Struct. Biol.* **180**, 519–530 (2012).

86. Kucukelbir, A., Sigworth, F. J. & Tagare, H. D. Quantifying the local resolution of cryo-EM density maps. *Nat. Methods* **11**, 63–65 (2014).

87. Afonine, P. V. *et al.* Real-space refinement in PHENIX for cryo-EM and crystallography. *Acta Crystallogr. Sect. Struct. Biol.* **74**, 531–544 (2018).

88. Mirdita, M. *et al.* ColabFold: making protein folding accessible to all. *Nat. Methods* **19**, 679–682 (2022).

89. Goddard, T. D. *et al.* UCSF ChimeraX: Meeting modern challenges in visualization and analysis. *Protein Sci. Publ. Protein Soc.* **27**, 14–25 (2018).

90. Moggridge, S., Sorensen, P. H., Morin, G. B. & Hughes, C. S. Extending the Compatibility of the SP3 Paramagnetic Bead Processing Approach for Proteomics. *J. Proteome Res.* **17**, 1730–1740 (2018).

Acknowledgments

We thank the European Research Council (ERC-2018-StG-805230 to A.A.), the Medical Research Council UK (MR/T032154/1 to A. Maréchal). The cryo-EM facility is funded by the Knut and Alice Wallenberg, Family Erling Persson, and Kempe foundations.

Author contributions

A. Mühleip, L.S. and A.A. designed the project. F.W. and A.A. performed cell culturing, isolation of mitochondria and prepared the sample. F.W. collected and processed cryo-EM data and built the model. T.G., A. Maréchal and A.A. performed biochemical and spectroscopic analyses. F.W., A. Maréchal and A.A. wrote the manuscript.

Competing Interests Statement

The authors declare no competing interests.

SUPPLEMENTARY INFORMATION

Supplementary Fig. 1: Purification and biochemical characterization of the respirasome from *P. marinus*.

Supplementary Fig. 2: Cryo-EM image processing overview.

Supplementary Fig. 3: Map quality for individual complexes and states.

Supplementary Fig. 4: Endogenous structured lipids identified in the map.

Supplementary Fig. 5: Cartoon representation of the individual subunits forming CII.

Supplementary Fig. 6: Cartoon representation of the individual subunits and associated proteins of CIII.

Supplementary Fig. 7: Newly modeled subunits in the SC.

Supplementary Fig. 8: Cartoon representation of the individual subunits forming CIV.

Supplementary Fig. 9: Multi-body refinement analysis.

Supplementary Fig. 10: Lipids interaction with COX39, COX40, and QCR8.

Supplementary Fig. 11: Protein interaction map between complexes.

Supplementary Fig. 12: Diversity of respiratory SCs.

Supplementary Fig. 13: Protein lipids interactions at the II:III interface.

Supplementary Fig. 14: Subunits and interactions in CII.

Supplementary Fig. 15: Electrostatic surface potential of SC, ISPR1,2 and Cyt *c*.

Supplementary Fig. 16: Parasite-specific subunit QCR11 substitutes the mammalian N-terminal partner RIP1-2.

Supplementary Fig. 17: BLASTP hits for ISPR1 and identification of a putative ISPR2 homologue in *T. gondii*.

Supplementary Fig. 18: Interactions between the farnesyl tail of heme *a* and the tail of CDL 32 in CIV.

Supplementary Fig. 19: *AlphaFold2*-predicted transmembrane domain of CII.

Supplementary Fig. 20: Protein splitting in COX2 and frameshifts in the mitochondria-encoded proteins COX1, Cyt *b*, COX3.

Supplementary Table S1 and S2: Cryo-EM data collection, refinement, and validation statistics.

Supplementary Table S3: List of modeled proteins.

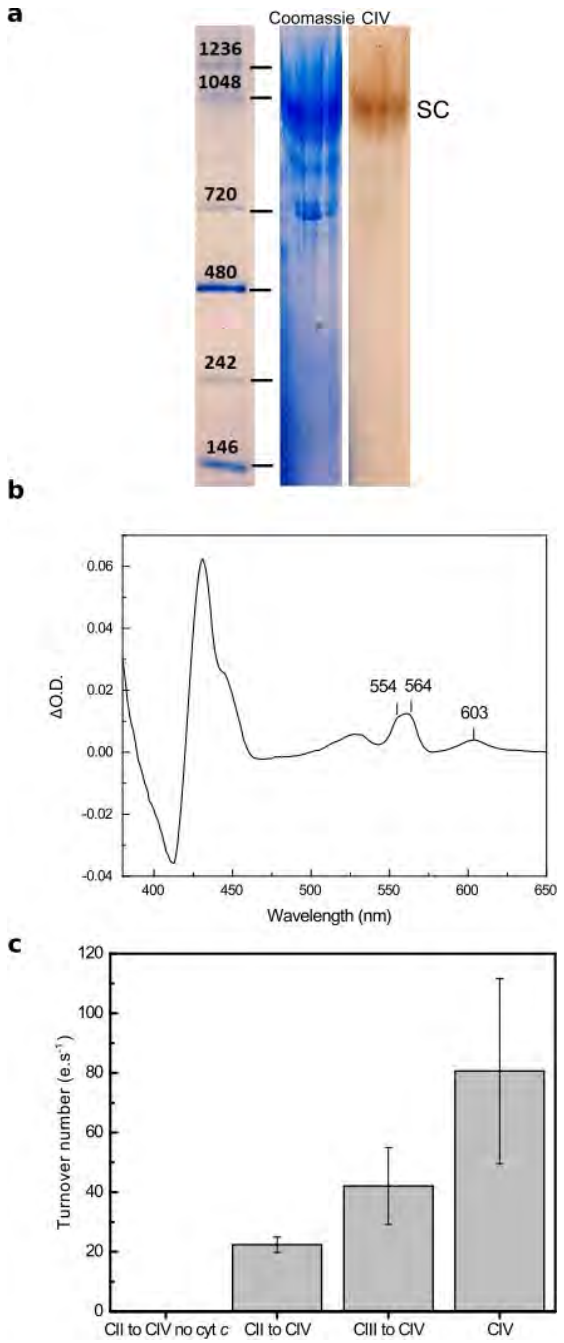

Supplementary Fig. 1: Purification and biochemical characterization of the respirasome from *P. marinus*. a. Redox visible absorption spectrum of the SC sample obtained after sucrose cushion revealing the presence of C- (554 nm), B- (564 nm) and A- (603 nm) type hemes, characteristic for CIII and CIV. **b.** Turnover number ($e.s^{-1}$) measured for the SC on oxygen consumption with substrate succinate (CII to CIV no cyt *c*), with succinate and additional cyt *c* (CII to CIV), with substrate decyl QH_2 and cyt *c* (CIII to CIV), with cyt *c* and ascorbate and TMPD (CIV). Values given are means ± standard deviations.

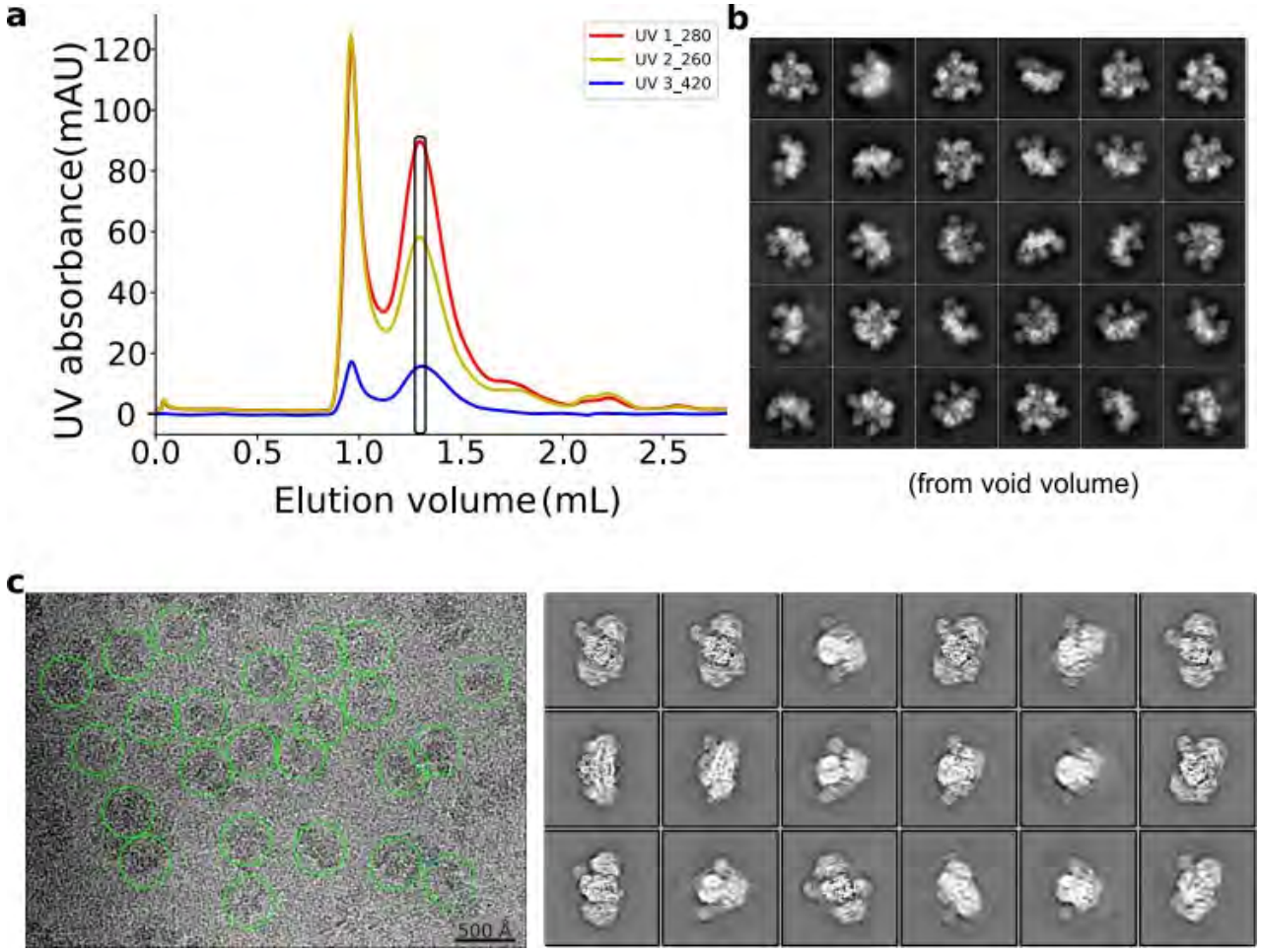
a
UV absorbance(mAU)
120
100
80
60
40
20
0
0.0
0.5
1.0
1.5
2.0
2.5
Elution volume(mL)
UV 1_280
UV 2_260
UV 3_420
b
(from void volume)
c
500 Å

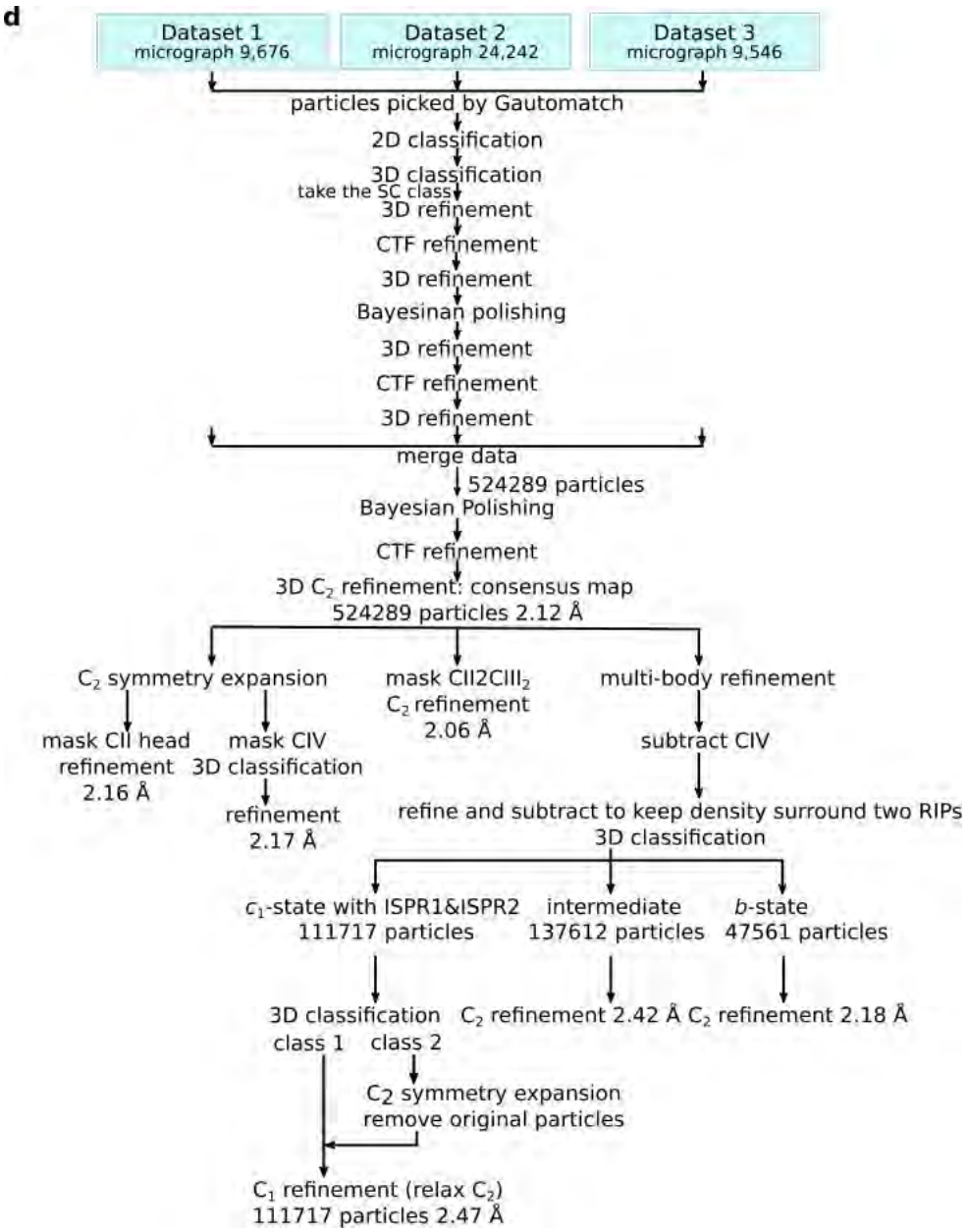

Supplementary Fig. 2: Cryo-EM image processing overview. a. Chromatogram of the Superose 6 Increase 3.2/300 column, the pooled fractions used for cryo-EM are indicated with a rectangle. **b.** 2D class averages of ATP synthase hexamers from void volume. **c.** A representative micrograph with picked particles (green circles). 2D class averages of SC. **d.** Data processing scheme for the complete SC II2-CIII$_2$-IV2, CII head, CIV, CII2CIII$_2$, and CIII states c_1, *b*, and intermediate. A total of 43464 movies were recorded and analyzed, particles that were not SC were discarded by classification, since they cannot contribute to reconstruction. Consensus map was produced from 524289 particles. Cryo-EM structures were successfully obtained from three preliminary datasets.

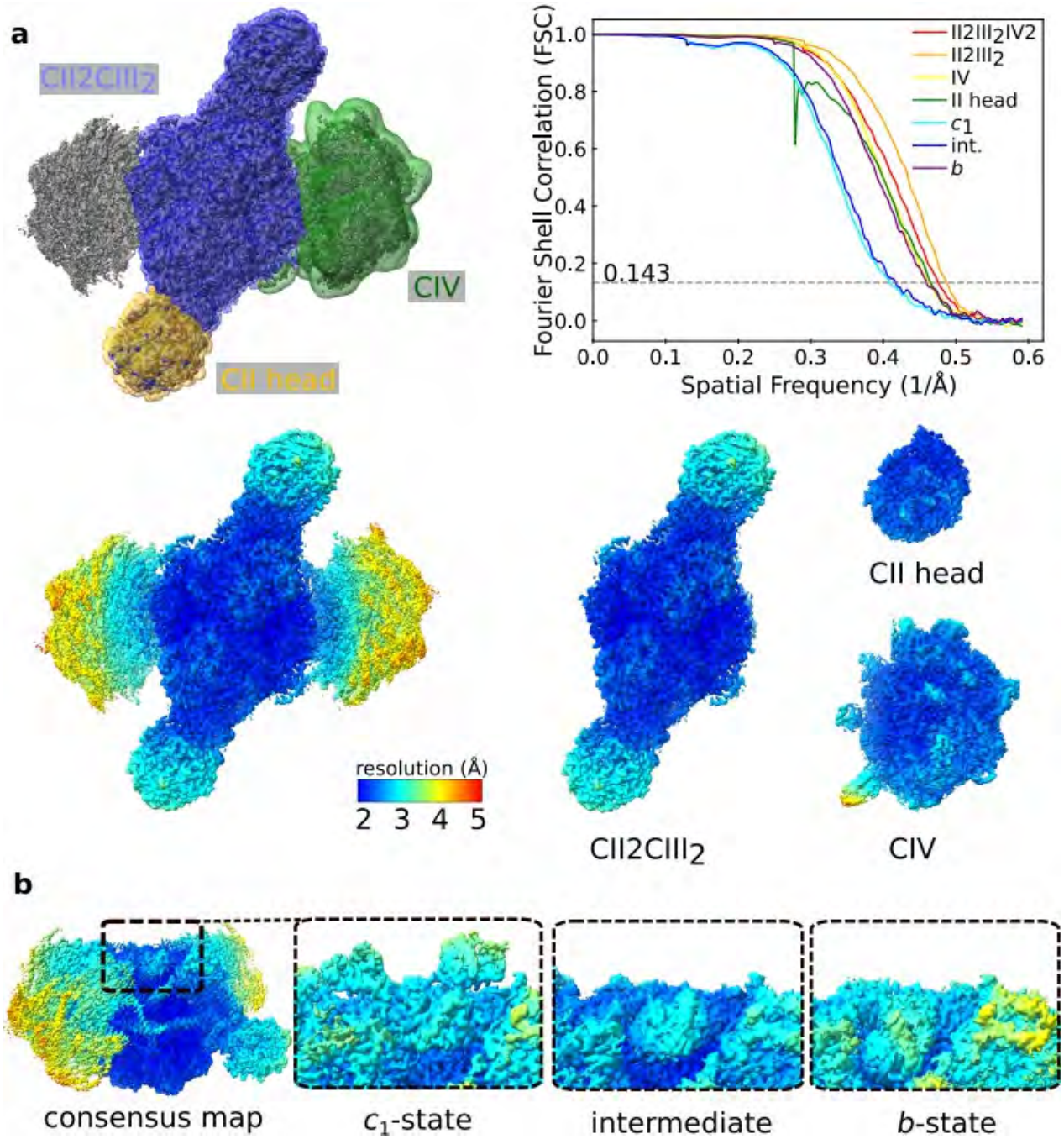

Supplementary Fig. 3: Map quality for individual complexes and states.
a. Binary masks used for local masked refinements of CII2CIII2, CIV, and CII head. Fourier Shell Correlation curves of the half maps and local-masked refinements. Cryo-EM map resolution estimates by Fourier Shell Correlation were performed using half maps from random half-sets. Consensus map colored by local resolution. Local-masked refinements colored by local resolution.
b. Local resolution of maps for RIP1 when in c_1,*b*, and intermediate states.

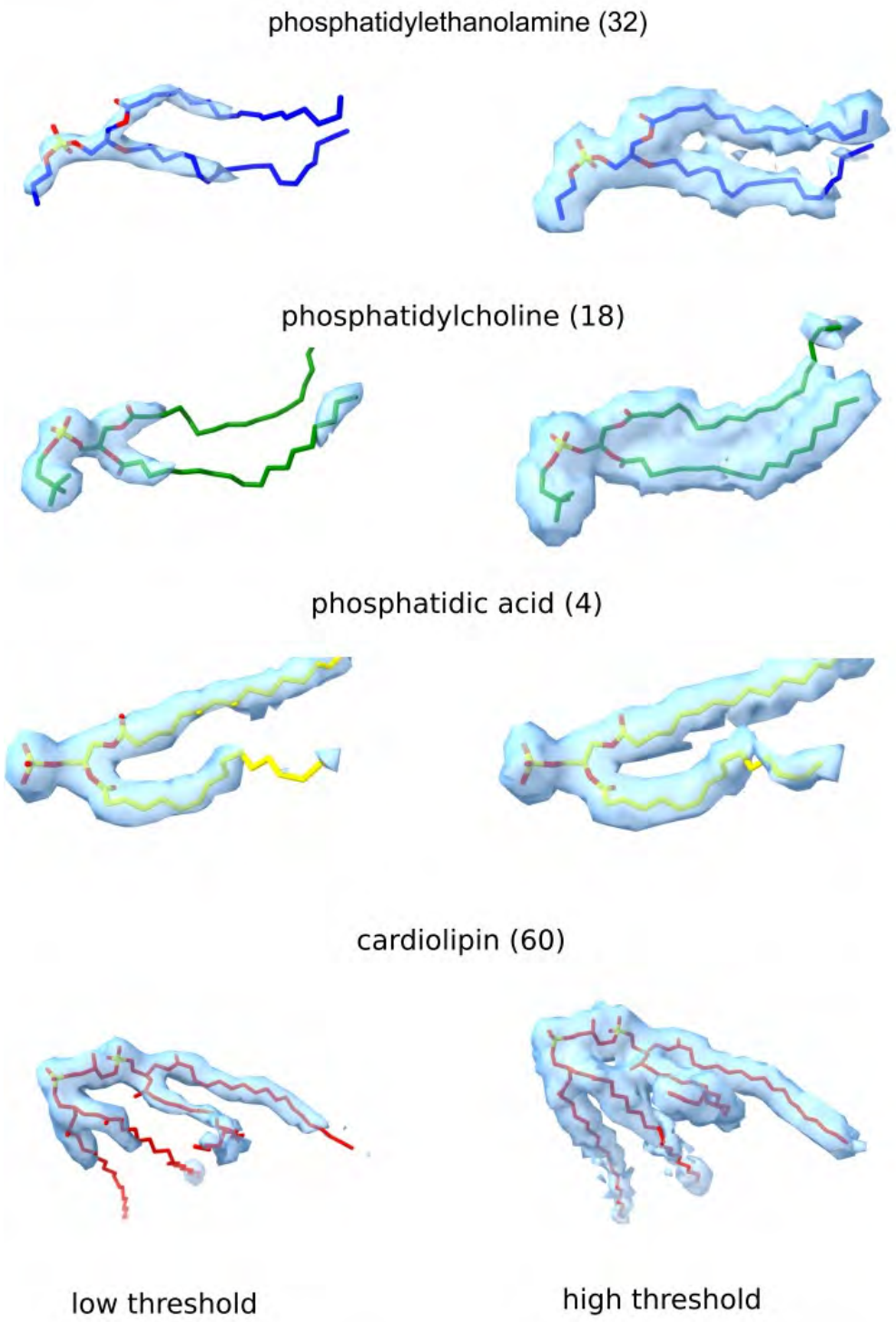

Supplementary Fig. 4: Endogenous structured lipids identified in the map.

Four types of lipids are shown with their densities in two different thresholds. For each type, the number of modeled lipids is indicated in the brackets.

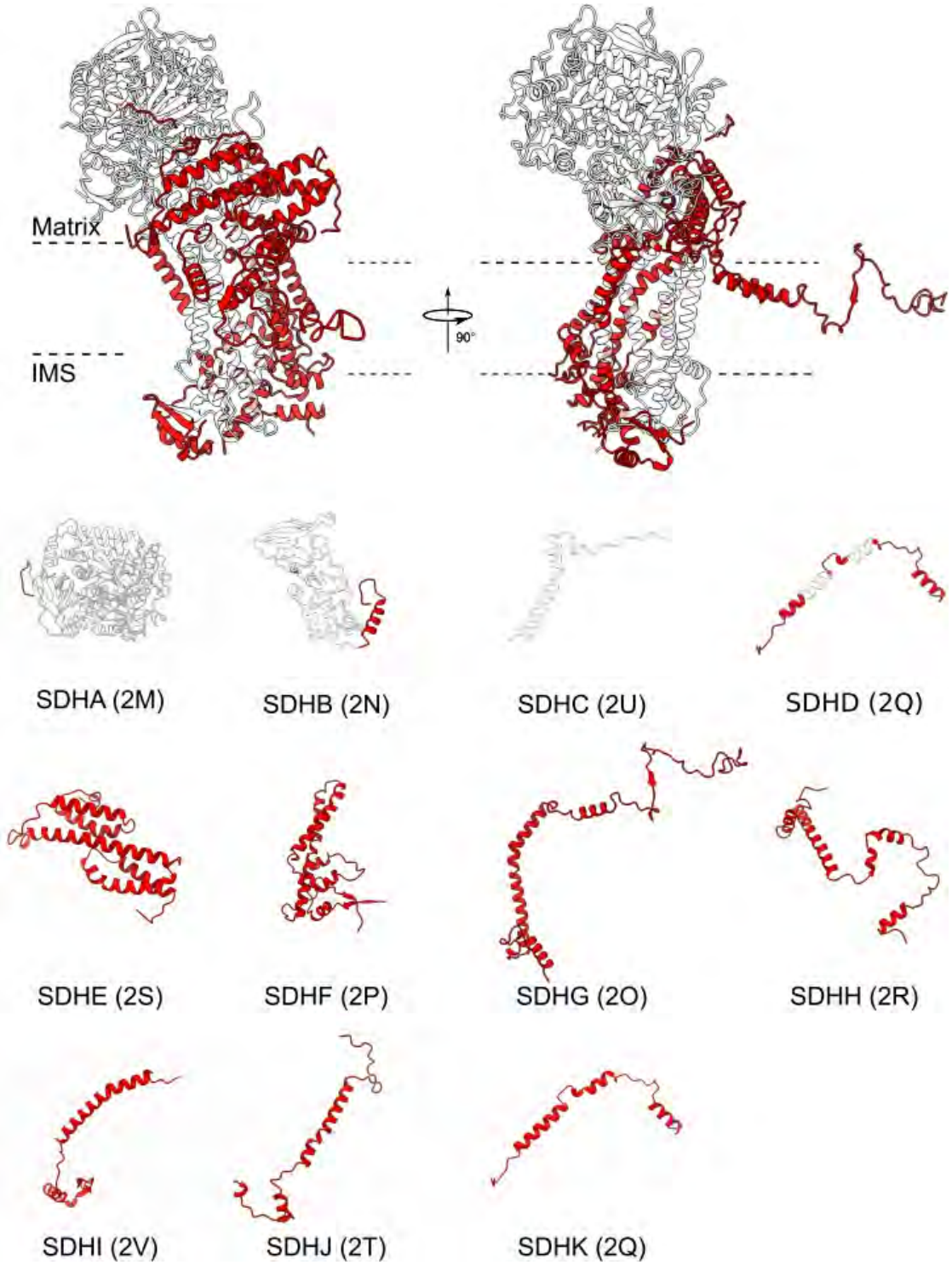

Supplementary Fig. 5: Cartoon representation of the individual subunits forming CII. Tertiary folds of all the built components are shown. Conserved structures with the canonical (mammalian) CII are in white; extensions and specific proteins are in red. Chain IDs are indicated.

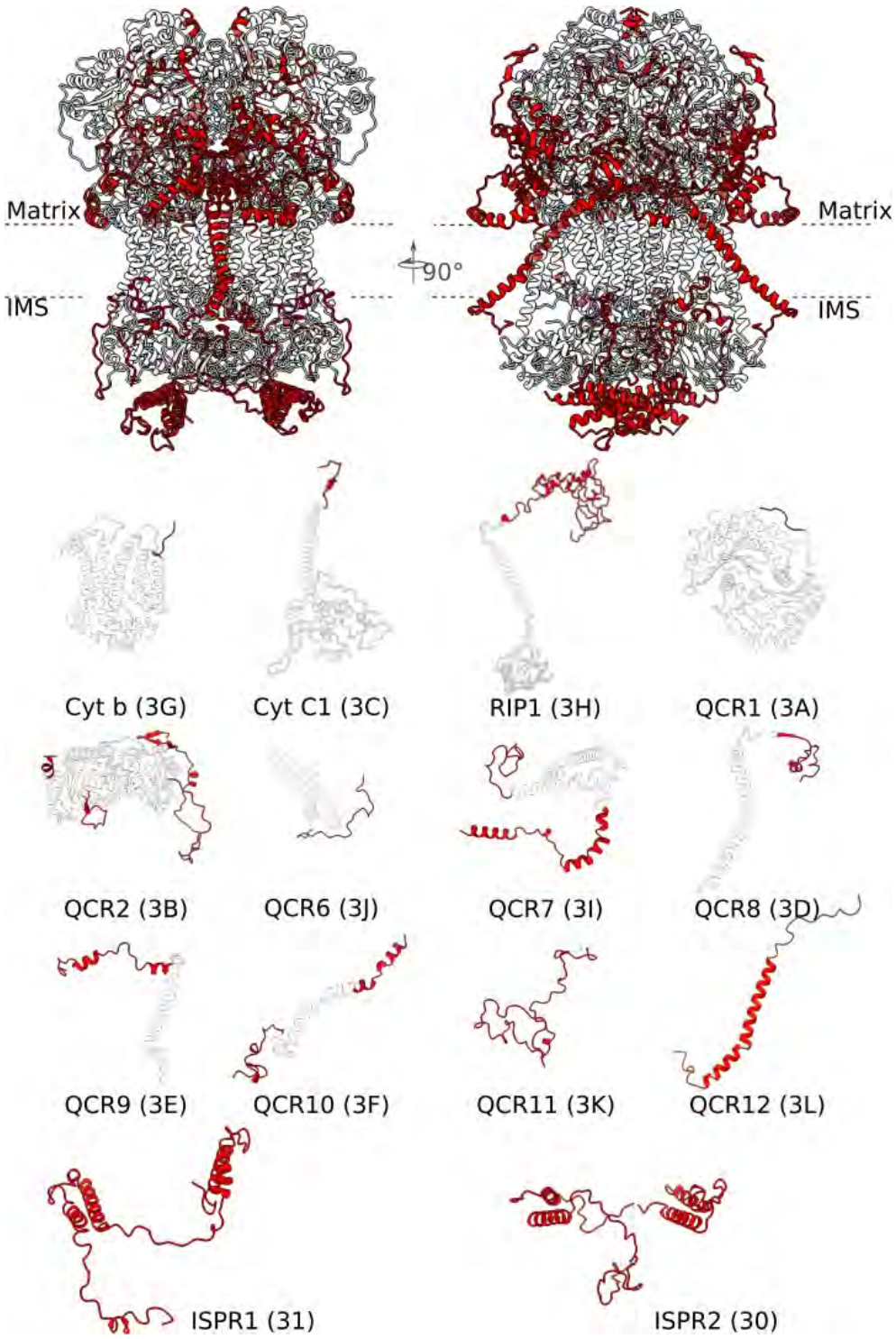

Supplementary Fig. 6: Cartoon representation of the individual subunits and associated proteins of CIII. Tertiary folds of all the built components are shown. Conserved structures with the canonical (mammalian) CIII are in white; extensions and specific proteins are in red. Chain IDs are indicated.

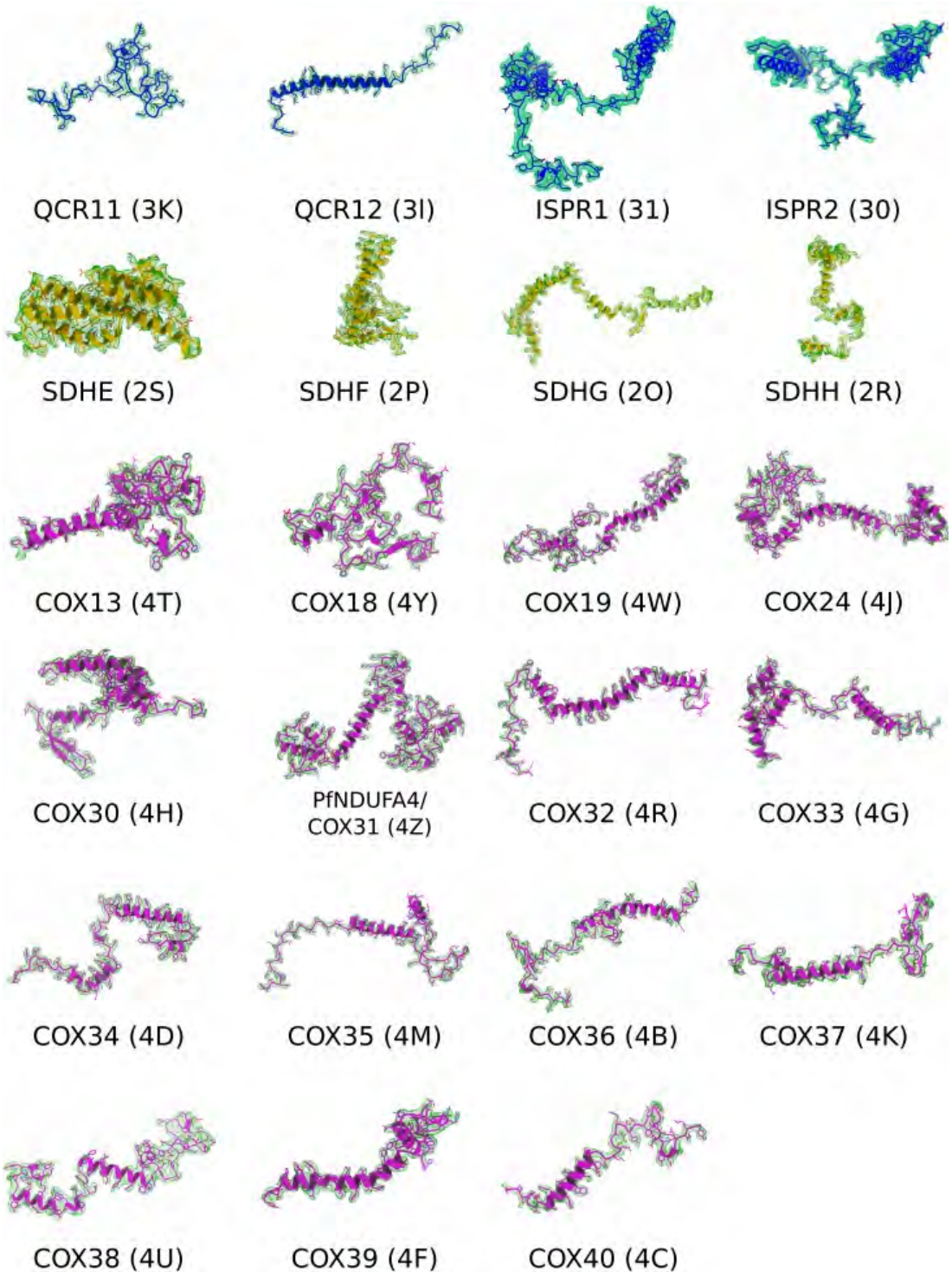

Supplementary Fig. 7: Newly modeled subunits in the SC. Specific subunits identified directly from the complex in which they associate. CII yellow, CIII blue, CIV magenta. The ISPR1 and ISPR2 heterodimer occupies the Cyt *c* electron acceptor binding site.

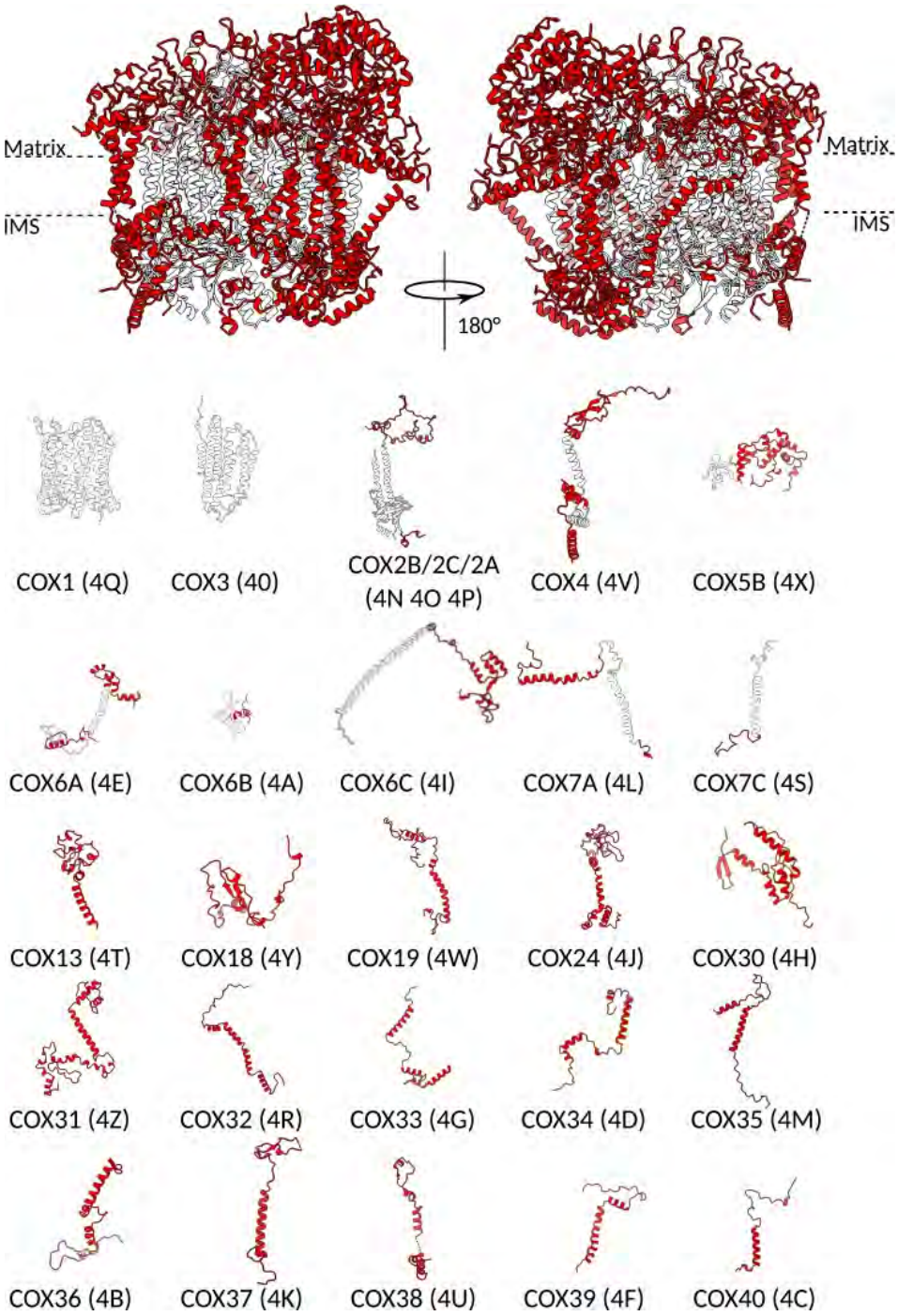

Supplementary Fig. 8: Cartoon representation of the individual subunits forming CIV. Tertiary folds of all the built components are shown. Conserved structures with the canonical (mammalian) CIV are in white; extensions and specific proteins are in red. Chain IDs are indicated.

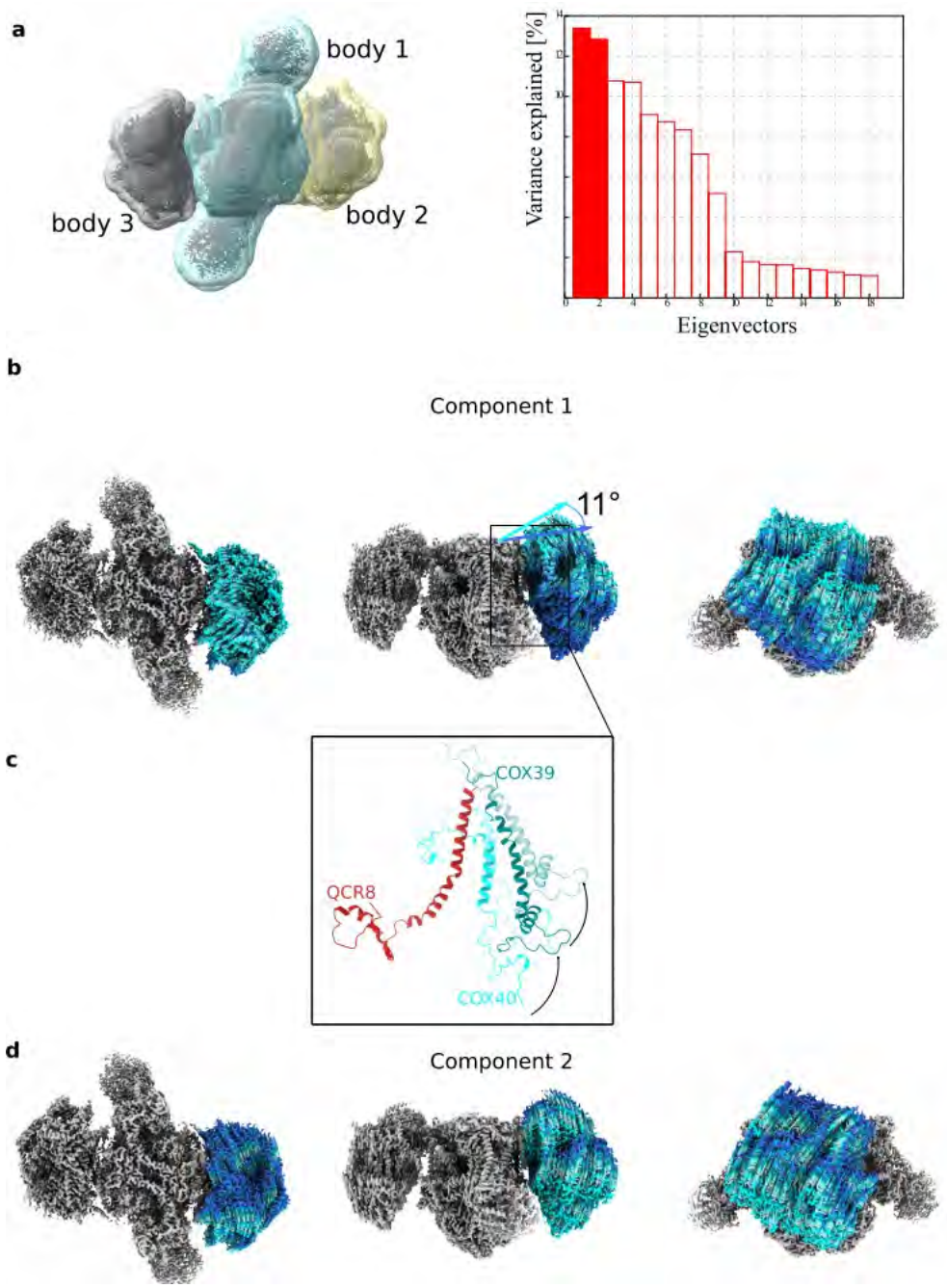

Supplementary Fig. 9: Multi-body refinement analysis. a. Three masks used for multi-body refinement: body 1 – $CIII_2$, body 2 – CIV(1), body 3 – CIV(2). Eigenvectors that explain the variability of the data. The distribution of eigenvectors shows that none of them accounts for more than 14% of the motion. **b.** Top, front, and side views of the map, showing the motion along the component 1. **c.** The two extreme positions of COX39 and COX40 in relation to fixed QCR8 in component 1. **d.** Top, front, and side views of the map, showing the motion along the component 2

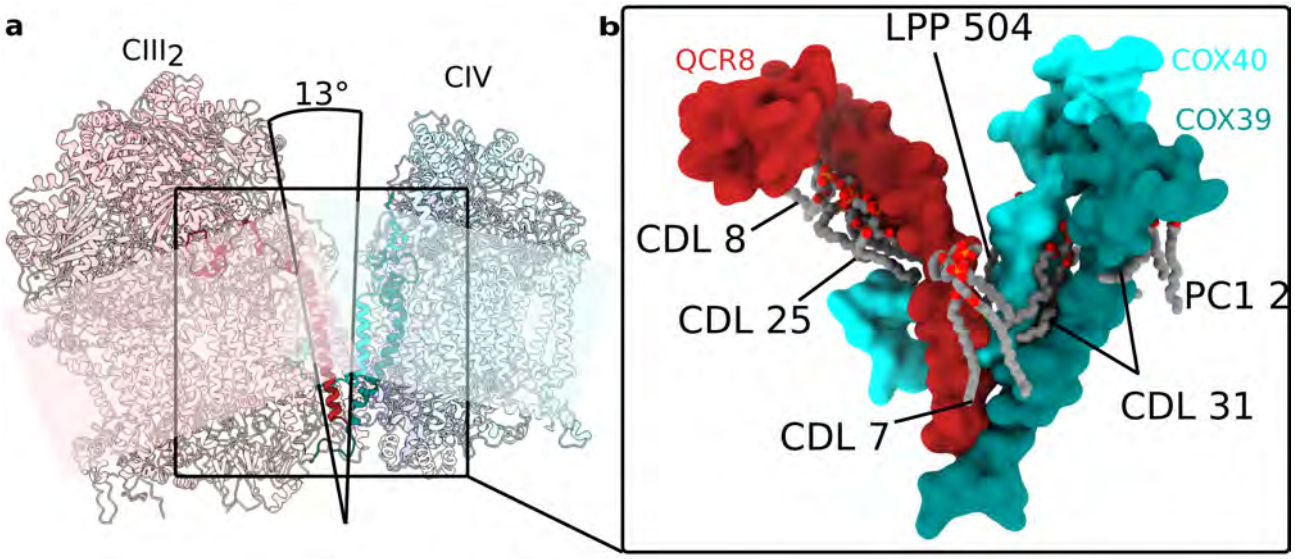

Supplementary Fig. 10: Lipids interaction with COX39, COX40, and QCR8.
a. The position of COX39, COX40, and QCR8 with lipids in the consensus structure, in which 13° angle formed by the V-shape association of $CIII_2$ and CIV in the consensus map. The membrane planes are indicated in the background. **b.** Lipids tightly interact with QCR8, COX39, and COX40 are shown.

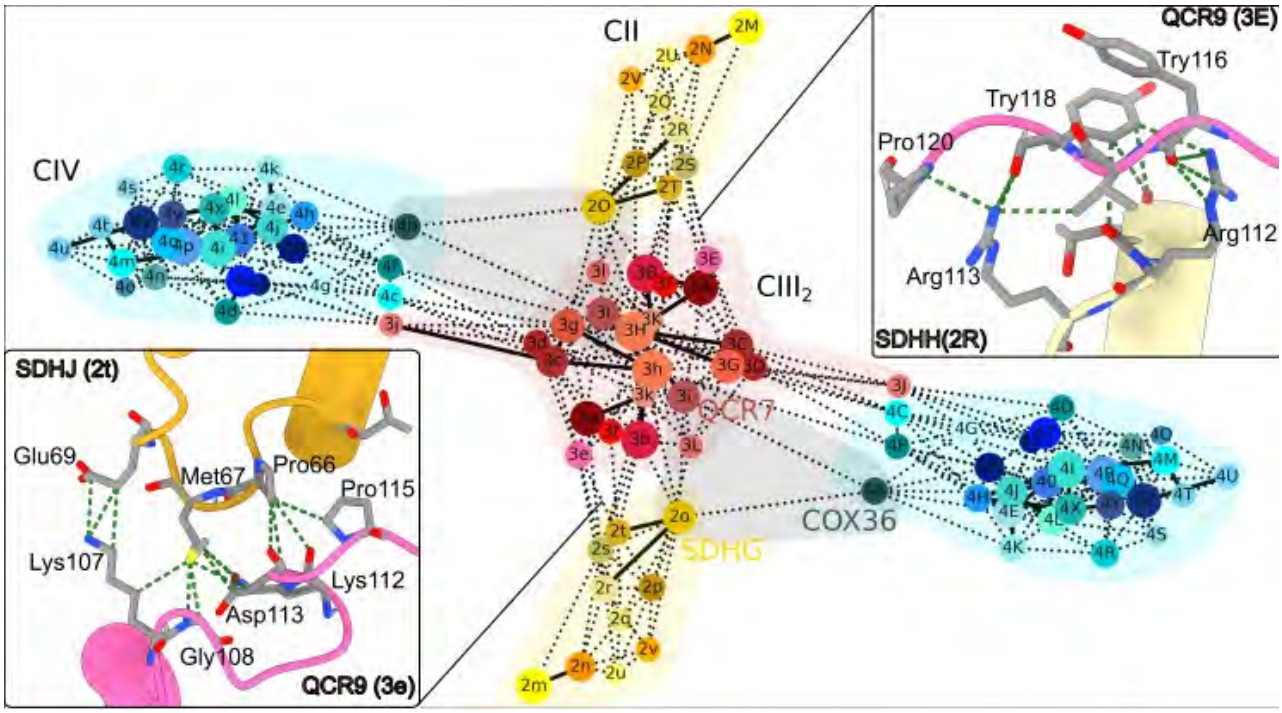

Supplementary Fig. 11: Protein interaction map between complexes.
Schematic of protein-protein interactions, where nodes correspond to individual proteins (chain IDs indicated) and colored in shades of yellow (CII), red (CIII), cyan (CIV). The interactions were calculated using probe radius 3 Å using ChimeraX (Goddard *et al.* 2018).

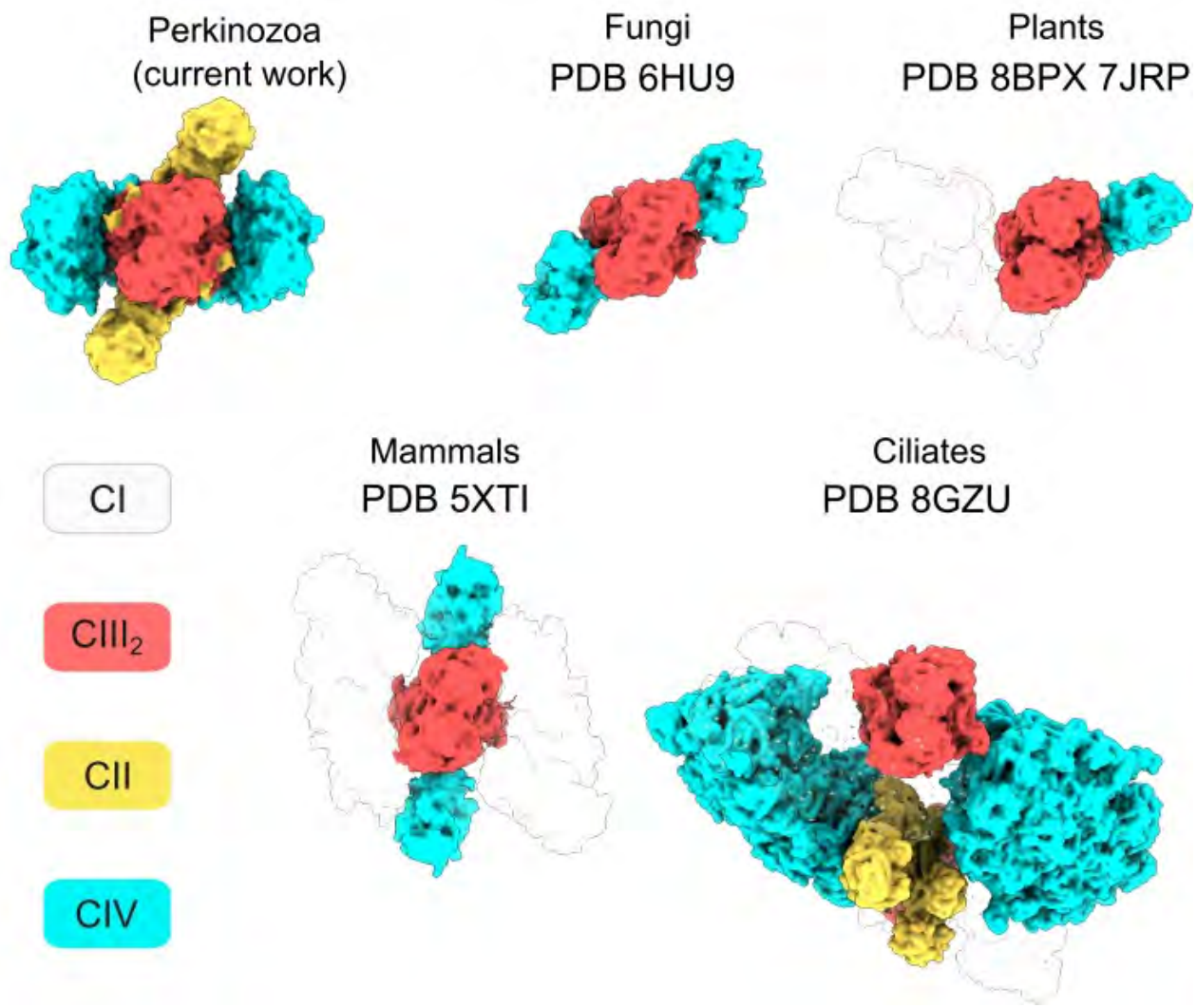

Supplementary Fig. 12: Diversity of respiratory SCs.
Comparison of known modes between SCs from Perkinsozoa, fungi, plants, mammals, and ciliates. All contain $CIII_2$ (red) and are shown in the same CIII orientation. PDB IDs of the models used are indicated.

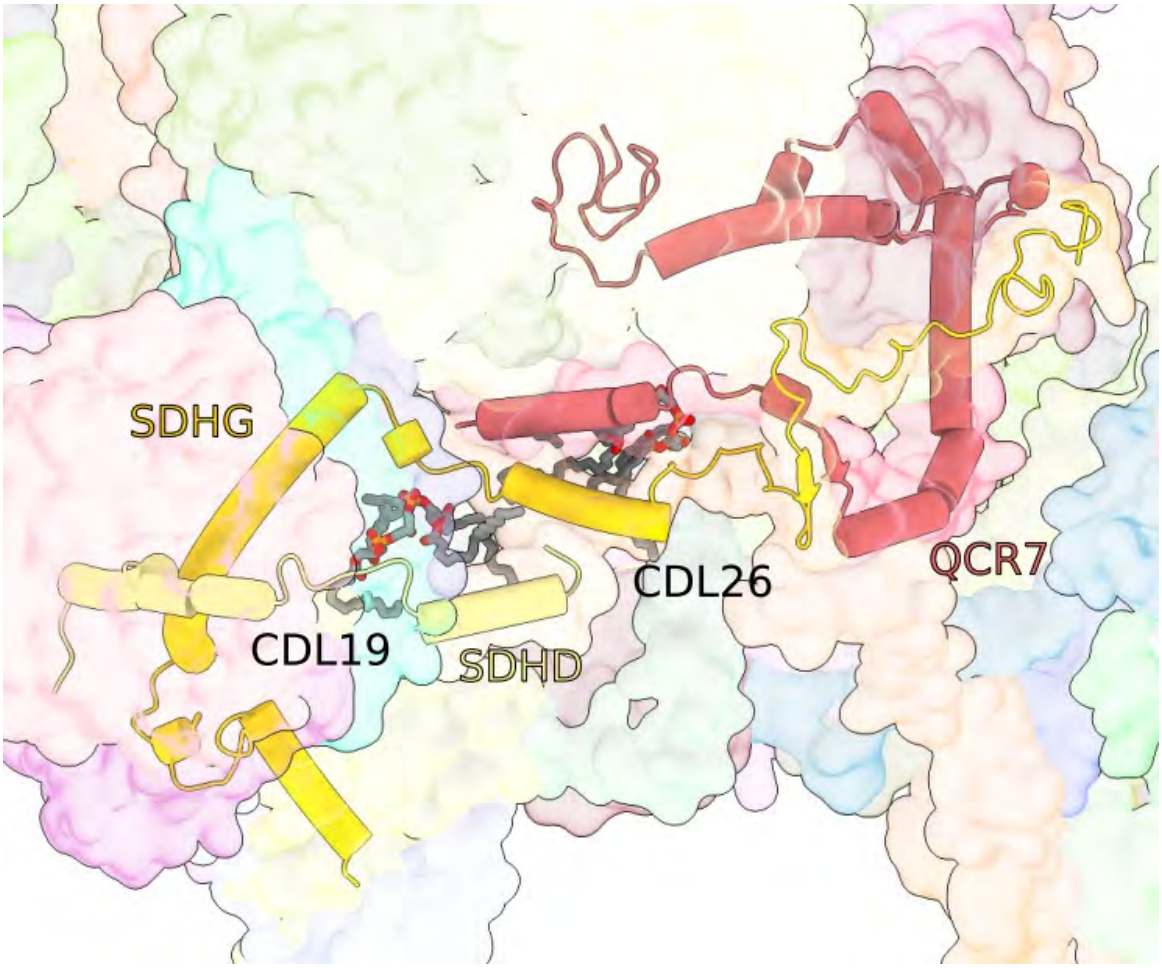

Supplementary Fig. 13: Protein lipids interactions at the II:III interface.
Lipids CDL19 and CDL26 interact with SDHD and SHDG of CII and QCR7 of CIII, highlighting cardiolipin impliation in the SC formation.

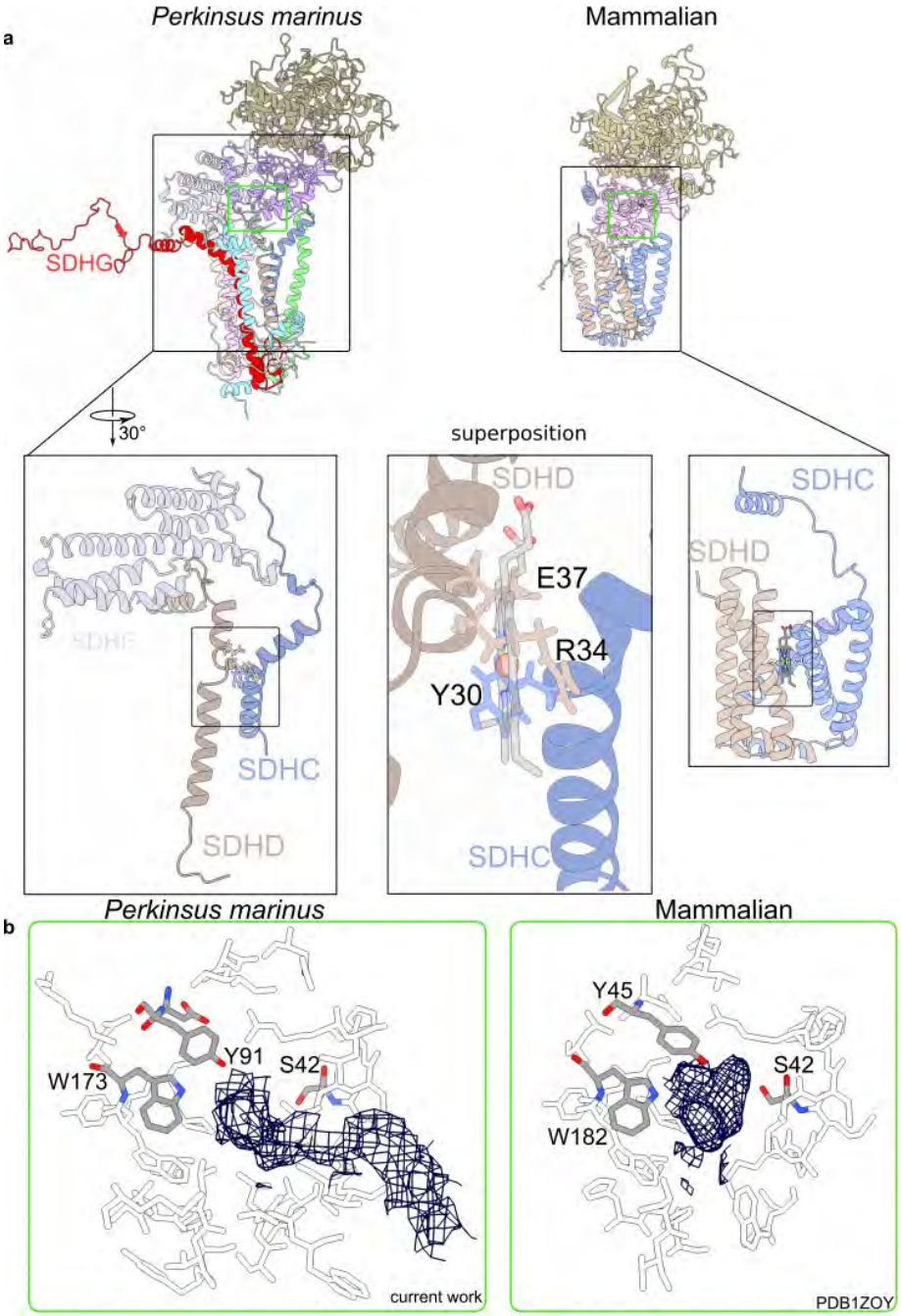

Supplementary Fig. 14: Subunits and interactions in CII. a. Comparison of CII structures between *Perkinsus* (current work) and mammals (PDB 1ZOY). Close-up views show the membrane-anchoring module SDHC-SDHD. SDHC-SDHD had not been not previously identified in Apicomplexa due to the divergent and truncated sequences. The superposition shows the the helices that contribute axial ligands to the heme group in mammals adopt a different conformation in *Perkinsus*, and that the prosthetic group is not compatible with our structure. **b.** Conserved residues in the quinone binding site of CII. Density for quinone is represented in black mesh in the site.

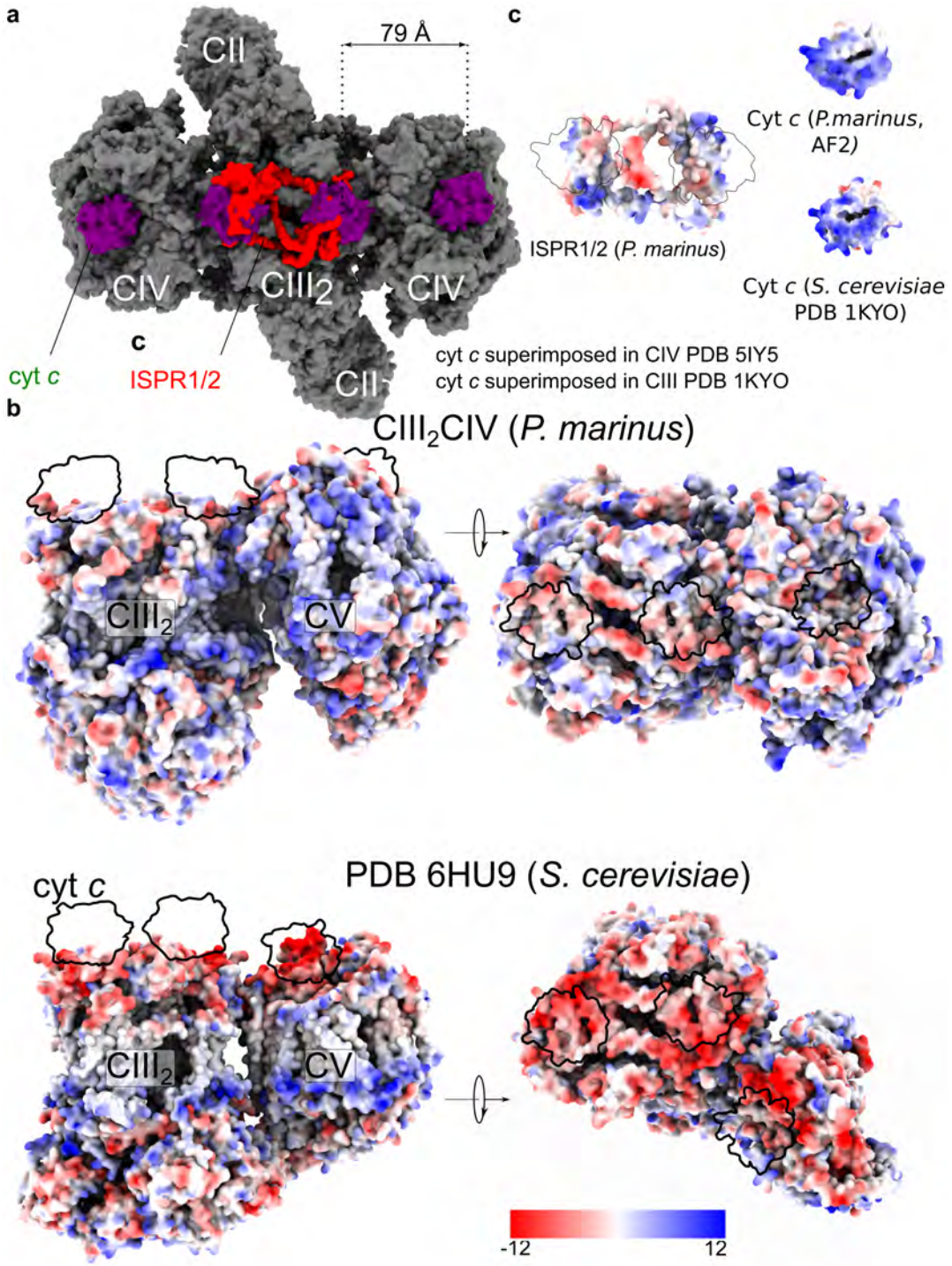

Supplementary Fig. 15: Electrostatic surface potential of SC, ISPR1,2 and Cyt *c*.

a. Clashes between Cyt *c* and ISPR1,2 on the surface of the SC. The distance of the docking site for Cyt *c* between CIII and CIV is 79 Å. **b.** Comparison of the relative static electron potential surface of CIII-CIV between *P. marinus* and *S. cerevisiae*. **c.** Comparison of the surface of ISPR1,2 and Cyt *c* that interacts with CIII.

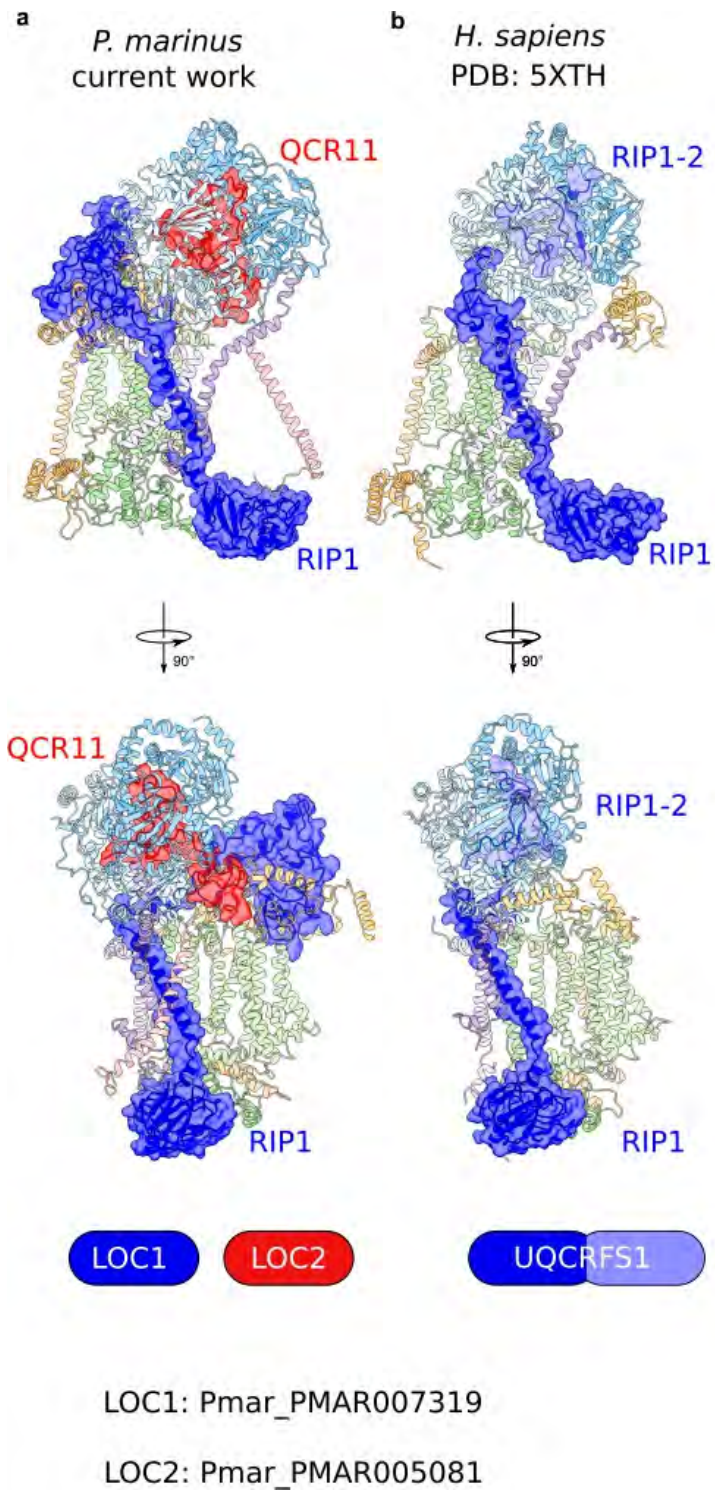

Supplementary Fig. 16: Parasite-specific subunit QCR11 substitutes the mammalian N-terminal partner RIP1-2. a. *P. marinus* RIP1 is blue, QCR11 is red. **b.** *H. Sapiens* RIP1 is blue, RIP1-2 is light blue.

a ISPR1 (chain 31) NCBI BLASTP hits agains none-*Perkinsus* species

Scientific Name	Max Score	Total Score	Query Cover	E value	Per. Ident	Acc. Len	Accession
Neospora caninum Liverpool	87	87	93%	6e-18	30.32%	162	CEL69052.1
Toxoplasma gondii ME49	84	84	93%	1e-16	29.68%	162	XP_018635966.1
Besnoitia besnoiti	82.4	82.4	93%	4e-16	31.61%	164	XP_029219297.1
Cardiosporidium cionae	82	82	98%	6e-16	32.72%	163	KAF8822737.1
Cystoisospora suis	78.6	78.6	93%	1e-14	31.41%	162	PHJ25754.1
Neospora caninum Liverpool	80.9	80.9	89%	5e-14	30.20%	1546	XP_003884378.1
Cardiosporidium cionae	75.5	75.5	78%	7e-14	35.20%	124	KAF8823100.1
Eimeria brunetti	76.6	76.6	81%	8e-14	31.11%	176	CDJ49398.1
Cyclospora cayetanensis	76.3	76.3	85%	1e-13	31.94%	176	XP_022590310.2
Cyclospora cayetanensis	76.3	76.3	85%	1e-13	31.94%	178	OEH77517.1
Polarella glacialis	76.3	76.3	77%	2e-13	27.38%	197	CAE8623700.1
Symbiodinium pilosum	56.6	56.6	30%	3e-07	51.02%	65	CAE7747229.1

b

```
224932* T. gondii      ----------------------------------------
ISPR1   P. marinus     ----------------------------------------
ISPR2   P. marinus   1 AGRALEDSTSDISTWAASSLASGAYEATEGAGTPAGGGGAAA  42

224932* T. gondii    1 MDRYFSANCREELQGHVNCAKVFLEQHVKFGTPYLPGSDDG-  41
ISPR1   P. marinus   1 ---SFTPTCNKELTAHIDCVKSFLREARTKHTPYLPGTGAAA  39
ISPR2   P. marinus  43 AAAAYSANCRDELNSHVECVKAFLRLSAAGGGAAGGGGGGGY  84
                            α1                          α2

224932* T. gondii   42 ADPCRTTRSLYMKCMQERKIHGLDGDKVALSLAQFSGPPKPC  83
ISPR1   P. marinus  40 ADKCSGSREYFAKCTMYAAA------TTSFRRTMSTEMPQPC  75
ISPR2   P. marinus  85 AAAAAAAAAAAA--------------AAAAAAAAAAAAEPPVC 112
                        α2

224932* T. gondii   84 EMELSMHGTCVANQLERTQKLGEK-----------YWTQGGE 114
ISPR1   P. marinus  76 EMELNLHGQCVGNYLTQSIRTGKAAAGA------ARGAAQSE 111
ISPR2   P. marinus 113 EAELTVHGSCVGQYLKNSILKRRPYPFLDPSYTGGEDNTYAD 154
                            α3

224932* T. gondii 115 DRCLVTRANYEQCMFRSLRGDSDSGNSSWQSAELEKNIGHLQ 156
ISPR1   P. marinus 112 DKCFLTRAAFEKCMMYQKITERATNEGQVEYADFSRRFGRQT 153
ISPR2   P. marinus 155 DKCFATRAQFEKCMLKKDI----------------------- 173
                            α4

224932* T. gondii 157 VKLPNK                                     162
ISPR1   P. marinus 154 QTTLGA                                     159
ISPR2   P. marinus     ------
```

* represents: TGME49_224932

Supplementary Fig. 17: BLASTP hits for ISPR1 and identification of a putative ISPR2 homologue in *T. gondii*.

a. Homologs of ISPR1 and ISPR2 in *Symbiodinium*, *Cyclospora*, *Toxoplasma* and *Neospora* species. **b.** The sequence alignment of *T. gondii* A0A125YMP1 with ISPR1, ISPR2, and. A0A125YMP1 and ISPR2 have C-terminal extensions.

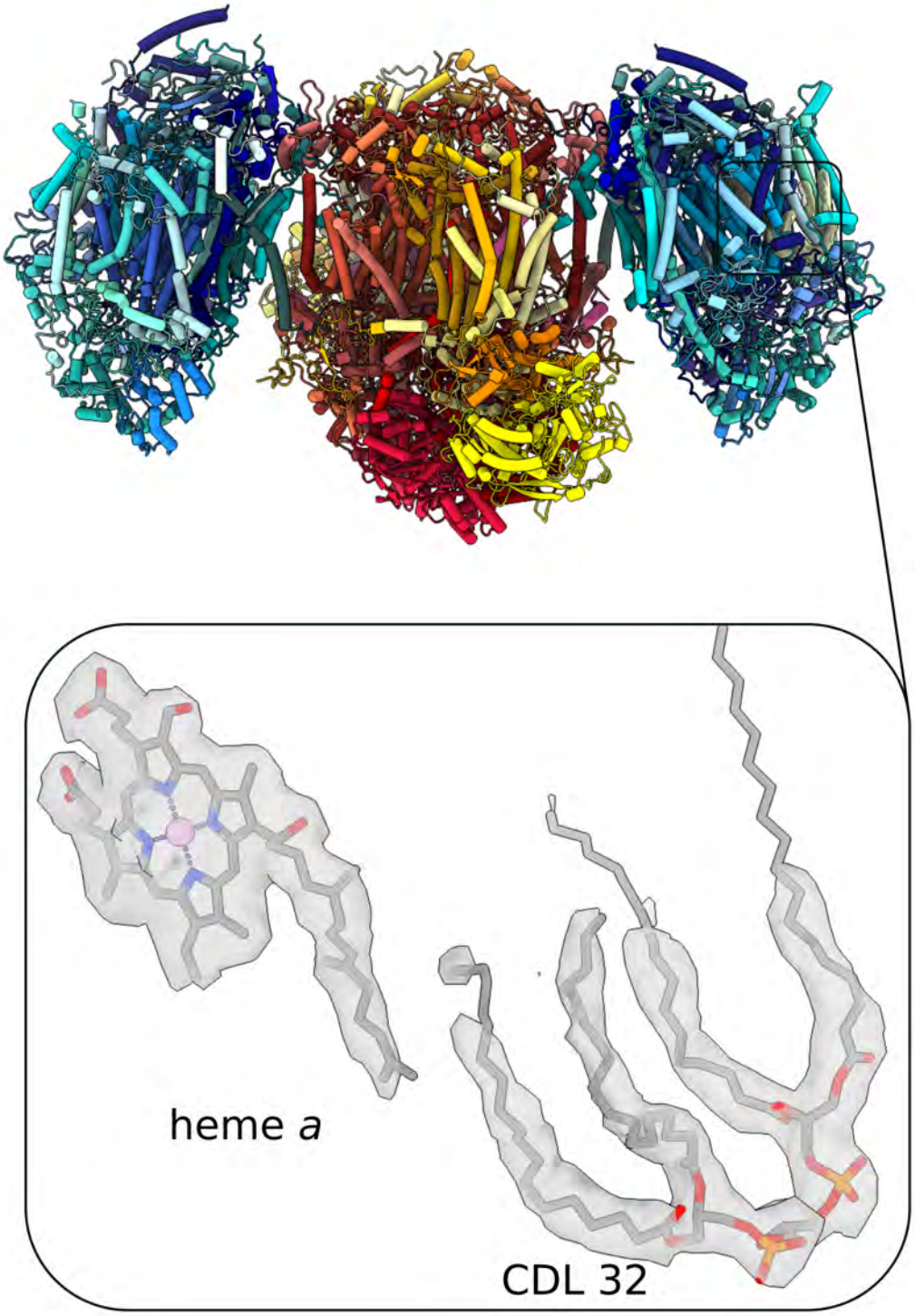

Supplementary Fig. 18: Interactions between the farnesyl tail of heme *a* and the tail of CDL 32 in CIV.
The long hydrocarbon chain of heme *a* helps anchoring heme *a* into the hydrophobic environment.

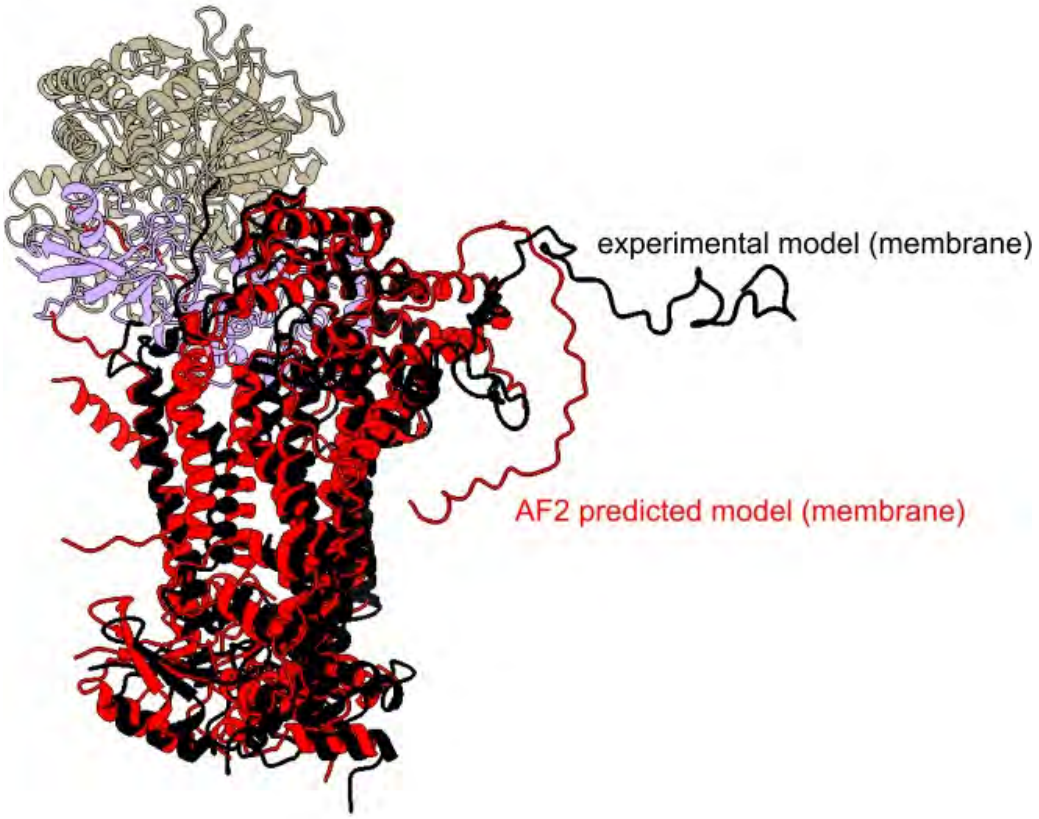

Supplementary Fig. 19: *AlphaFold2*-predicted transmembrane domain of CII.
The cryo-EM determined structure is shown in black cartoon and the predicted model in red.

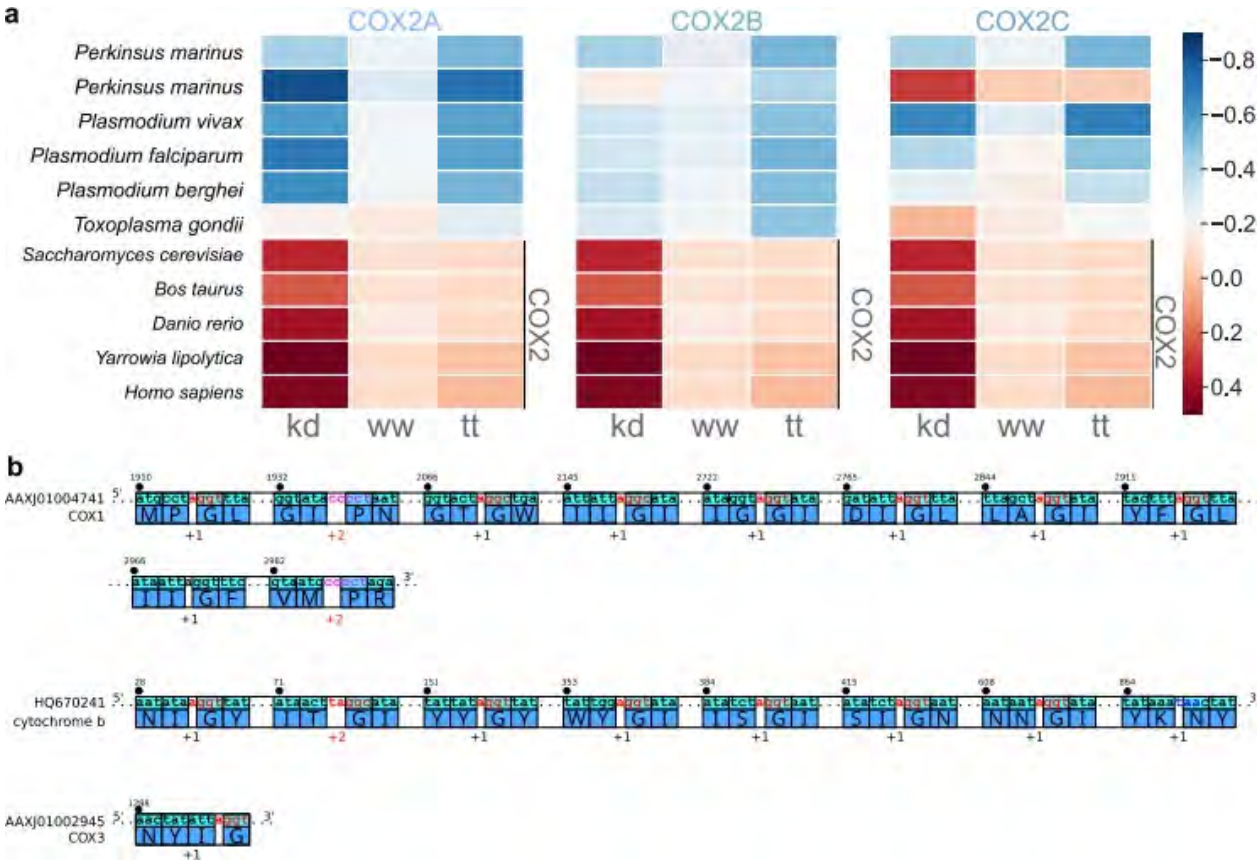

Supplementary Fig. 20: Protein splitting in COX2 and frameshifts in the mitochondria-encoded proteins COX1, Cyt *b*, COX3. a. Heat map indicating the average hydrophobicity of COX2 in divergent organisms, calculated as the grand average of hydropathy according to the Kyte-J.&Doolittle (kd) (Kyte and Doolittle, 1982), Moon-Fleming (mf) (Moon and Fleming, 2011) or Wimley-White (ww) (Wimley and White, 1996). **b.** Frameshifts found in mitochondria encoding three proteins COX1, COX3, and Cyt *b* with corresponding nucleotide and protein sequences.

Table S1: Cryo-EM data collection, refinement, and validation statistics (part 1)

	#1 c1 full map (EMDB-xxxx) (PDB xxxx)	#2 b full map (EMDB-xxxx) (PDB xxxx)	#3 int full map (EMDB-xxxx) (PDB xxxx)	#4 concensus (EMDB-xxxx)	#5 CII2CIII2 (EMDB-xxxx)
Data collection and processing					
Magnification	130 kx				
Voltage (kV)	300				
Electron exposure (e–/Å2)	17.2/24.71/23.75				
Defocus range (m)	0.3-1.5/0.3-5/0.5-2.0				
Pixel size (Å)	0.65/0.51/0.85				
Symmetry imposed	/	/	/	C2	C2
Initial particle images (no.)	/	/	/	210000	
Final particle images (no.)	/	/	/	296890	
Map resolution (Å)	/	/	/	2.18	2.1
-FSC threshold	/	/	/	0.143	0.143
Map resolution range (Å)	2.2-6.1	2.1-6.0	2.0-4.6	2.0-5.2	2.0-4.1
Map sharpening B factor (Å2)	/	/	/	-42.8002	-39.8104
Refinement					
Initial model used (PDB code)	/	/	/	/	/
Model resolution (Å)	2.5	0.5	0.5		
-FSC threshold	0.5	2.8	2.6	/	/
Model composition					
-Non-hydrogen atoms	142928	142374	142374	/	/
-Protein residues	16529	16186	16186	/	/
-Ligands	173	173	173	/	/
B factors (Å2)					
-Protein	35.66/96.29/56.30	2.22/111.04/57.39	2.22/111.04/57.39	/	/
-Ligand	37.08/97.09/60.02	31.17/78.42/60.96	31.17/78.42/60.96	/	/
R.m.s. deviations					
-Bond lengths (Å)	0.005	0.005	0.005	/	/
-Bond angles (°)	0.821	1.079	1.088	/	/
Validation					
-MolProbity score	1.24	1.2	1.27	/	/
-Clashscore	3.75	4.2	4.93	/	/
-Rotamers Outliers(%)	0.26	0.43	1.05	/	/
Ramachandran plot					

Table S1: Cryo-EM data collection, refinement, and validation statistics (part 1)

	#1 c1 full map (EMDB-xxxx) (PDB xxxx)	#2 b full map (EMDB-xxxx) (PDB xxxx)	#3 int full map (EMDB-xxxx) (PDB xxxx)	#4 concensus (EMDB-xxxx)	#5 CII2CIII2 (EMDB-xxxx)
-Favored (%)	97.63	98.32	98.24	/	/
-Allowed (%)	2.33	1.59	1.66	/	/
-Disallowed (%)	0.04	0.09	0.1	/	/

Table S2: Cryo-EM data collection, refinement, and validation statistics (part 2)

	#6 CIV (EMDB-xxxx)	#7 CII head (EMDB-xxxx)	#8 c1 CII2CIII2 (EMDB-xxxx)	#9 b CII2CIII2 (EMDB-xxxx)	#10 int CII2CIII2 (EMDB-xxxx)
Data collection and processing					
Magnification	130 kx				
Voltage (kV)	300				
Electron exposure (e–/Å2)	17.2/24.71/23.75				
Defocus range (m)	0.3-1.5/0.3-5/0.5-2.0				
Pixel size (Å)	0.65/0.51/0.85				
Symmetry imposed	C1	C1	C1	C2	C2
Initial particle images (no.)	210000				
Final particle images (no.)	296890		111717	47561	
Map resolution (Å)	2.2	2.2	2.5	2.5	2.2
FSC threshold	0.143	0.143	0.143	0.143	0.143
Map resolution range (Å)	2.1-4.7	2.1-3.2	2.2-6.1	2.1-6.0	2.0-4.6
Map sharpening B factor (Å2)	-32.6517	-51.3825	-31.9754	-29.3593	-31.7066

Table S3: Model building statistics by subunits

	Subunits	refseqProtein	UniProt ID	Gene	Resi built	Resi in total	Loca of sub-units	Comments
CII	SDHA	XP_002765468.1	C5LYE7	Pmar_PMAR002002	25-628	604	MA	Soluble head
	SDHB	XP_002765391.1	C5LYT4	Pmar_PMAR002387	22-280	259	ME	Soluble head
	SDHC	Not anotated	Not ano-tated	Nucleotide AAXJ01000691.1	1-48	48	ME	
	SDHD	XP_002787086[1]	C5K9W01	Pmar_PMAR0065061	3-71	69	ME	
	SDHE	XP_002777439.1	C5L1Y6	Pmar_PMAR013480	2-164	163	MA	
	SDHF	XP_002767545.1	C5LSM2	Pmar_PMAR017121	0-157	158	ME	
	SDHG	XP_002780482.1	C5KTH2	Pmar_PMAR001074	12-171	160	ME	
	SDHH	NA	NA	Nucleotide AAXJ01000252.1	0-116	117	ME	
	SDHI	XP_002773883.1	C5LCL6	Pmar_PMAR011745	0-86	87	ME	
	SDHJ	XP_002783522.1	C5KJI4	Pmar_PMAR001368	1-82	82	ME	
CIII	CytC1	XP_002787441.1	C5K8N0	Pmar_PMAR028703	38-278	241	MA	
	RIP1	XP_002778583.1	C5KYR8	Pmar_PMAR005081	24-349	326	MA	
	QCR1	XP_002771383.1	C5LJ83	Pmar_PMAR019976	23-476	454	MA	
	QCR2	XP_002780898.1	C5KS02	Pmar_PMAR025323	48-543	496	MA	
	QCR6	XP_002775032.1	C5L0W9	Pmar_PMAR002217, Pmar_PMAR008750, Pm_PMAR014855	2-65, 67-93	91	IMS	

QCR7	XP_002766250.1	C5LWC5	Pmar_PMAR026691	2-178	177	MA
QCR8	XM_002775212.1	C5L848	Pmar_PMAR003928	17-111	95	MA

[1]The first seven residues don't match the density.

	SubunitS	refseqProtein	UniProt ID	Gene	Resi built	Resi in total	Loca of sub-units	Comments
	QCR9	NA	NA	mRNA accession ID EH080768.1	29-120	92	MA	
	QCR10	XP_002780203.1	C5KTV6	Pmar_PMAR019102	1-84	84	MA, IMS	
	QCR11	NA	NA	Nucleotide AAXJ01000150.1	1-79	79	MA	Orthlog of human RIP1-2
	QCR12	NA	NA	Nucleotide AAXJ01000820.1	546-614	69	ME	
	Cytochrome b	ADZ98702.1 [1]	F8SRJ0	cob	0-352	353	MA	Mitchondrial genome encoded
CIV	COX1	NA	NA	Nucleotide AAXJ01004741.1	405-863	459	ME	
	COX2A	XP_002771104.1	C5LK31	Pmar_PMAR000912	26-205	180	IMS, ME, MA	
	COX2B	XP_002788613.1	C5K4Y7	Pmar_PMAR010143	30-160	131	IMS	
	COX2C	XP_002772446.1	C5LG07	Pmar_PMAR021765	355-401	47	ME	
	COX3	NA	NA	Nucleotide AAXJ01002945.1	15-114	100	ME	
	COX4	XP_002768221.1	C5LR54	Pmar_PMAR003010	-7-177	185	IMS, ME, MA	
	COX5B	XP_002766928.1	C5LUB2	Pmar_PMAR010908	33-258	226	MA	

COX6A	XP_002777788.1	C5L0U1	Pmar_PMAR008723	2-153	152	IMS, ME
COX6B	XP_002778986.1	C5KXQ7	Pmar_PMAR000825	15-114	100	IMS

[1]ADZ98702.1.fa add some residues at the beginning based on the DNA genome seq from ”scf_1104296930962 dna supercontig supercontig JCVI_PMG_1.0 scf_1104296930962 1 830 1 REF.dna”(database is from EnsemblProtists)

SubunitS	refseqProtein	UniProt ID	Gene	Resi built	Resi in total	Loca of sub-units	Comments
COX6C	XP_002768512.1	C5LPW2	Pmar_PMAR017244	42-237	196	IMS, ME, MA	
COX7A	XP_002781865.1	C5KPD1	Pmar_PMAR016315	11-132	122	IMS, ME, MA	
COX7C	XP_002768605.1	C5LPK3	Pmar_PMAR004196	2-66	65	IMS, ME, MA	
COX13	XP_002788524.1	C5K4P8	Pmar_PMAR010054	33-153	121	ME, MA	
COX18	XP_002788613.1	C5K4Y7	Pmar_PMAR010143	30-160	131	MA	
COX19	XP_002777809.1	C5L0W2	Pmar_PMAR008743	11-151	141	IMS, ME, MA	
COX24	XP_002775031.1	C5L533	Pmar_PMAR002216	18-203	186	IMS, ME, MA	
COX30	XP_002776302.1	C5L559	Pmar_PMAR014882	18-158	141	MA	
COX31	XP_002765270.1	C5LYX8	Pmar_PMAR016057	15-200	186	IMS, ME, MA	PfNDUFA4, Annotation correction
COX32	XP_002780528.1	C5KSX3	Pmar_PMAR001120	17-119	103	IMS, ME, MA	
COX33	XP_002779074.1	C5KJE7	Pmar_PMAR018803	3-102	100	IMS, ME	C4AP2
COX34	XP_002766970.1	C5LUF4	Pmar_PMAR010950	2-91	90	IMS, ME	C4AP1
COX35	XP_002773275.1	C5LDS7	Pmar_PMAR026525	5-102	98	IMS, ME, MA	C4AP3

SubunitS	refseqProtein	UniProt ID	Gene	Resi built	Resi in total	Loca of sub-units	Comments
COX36	XP_002785279.1	C5KED7	Pmar_PMAR009509	1-93	93	IMS, ME	Transmemberae part reaches into CIII, close to SDHG
COX37	XP_002780494.1	C5KST9	Pmar_PMAR001086	10-102	93	IMS, ME, MA	
COX38	XP_002772503.1	C5LG64	Pmar_PMAR021826	354-444	91	IMS, ME, MA	
COX39	XP_002786224.1	C5KBY9	Pmar_PMAR019904	77-161	85	IMS, ME	
COX40	XP_002774805.1	C5L7H1	Pmar_PMAR020595	1-75	75	ME, MA	N-term teaches into CIII

NA = Not annotated.
MA = Matrix
ME = Membrane
IMS = Inner membrane space (crista lumen).

References

J. Kyte and R. F. Doolittle. A simple method for displaying the hydropathic character of a protein. *Journal of Molecular Biology*, 157(1):105–132, May 1982.

C. Preston Moon and Karen G. Fleming. Side-chain hydrophobicity scale derived from transmembrane protein folding into lipid bilayers. *Proceedings of the National Academy of Sciences*, 108(25):10174–10177, June 2011.

W. C. Wimley and S. H. White. Experimentally determined hydrophobicity scale for proteins at mem- brane interfaces. *Nature Structural Biology*, 3(10):842–848, October 1996.

Goddard, T. D. *et al.* UCSF ChimeraX: Meeting modern challenges in visualization and analysis. *Protein Sci. Publ. Protein Soc.* **27**, 14–25 (2018).